UCRL 9752

UNIVERSITY OF CALIFORNIA

Ernest O. Lawrence Radiation Laboratory

HYPERON PRODUCTION BY K^- MESONS INCIDENT ON HYDROGEN

TWO-WEEK LOAN COPY

This is a Library Circulating Copy which may be borrowed for two weeks. For a personal retention copy, call Tech. Info. Division, Ext. 5545

DISCLAIMER

This document was prepared as an account of work sponsored by the United States Government. While this document is believed to contain correct information, neither the United States Government nor any agency thereof, nor the Regents of the University of California, nor any of their employees, makes any warranty, express or implied, or assumes any legal responsibility for the accuracy, completeness, or usefulness of any information, apparatus, product, or process disclosed, or represents that its use would not infringe privately owned rights. Reference herein to any specific commercial product, process, or service by its trade name, trademark, manufacturer, or otherwise, does not necessarily constitute or imply its endorsement, recommendation, or favoring by the United States Government or any agency thereof, or the Regents of the University of California. The views and opinions of authors expressed herein do not necessarily state or reflect those of the United States Government or any agency thereof or the Regents of the University of California.

TECHNICAL INFORMATION DIVISION

Lawrence Radiation Laboratory

Berkeley

INFORMATION DIVISION
LAWRENCE RADIATION LABORATORY
UNIVERSITY OF CALIFORNIA
BERKELEY, CALIFORNIA

Assigned to

Loan to

Route to	Noted
P. Berlin	JUN 6 1962
C Schultz	MAR 14 1963
U CAMERINI	
Geo. Kalmus	JUN 21 1966
50A - 2137	
A. Veyler.	

Please return this document to the Information Division. Do not send it to the next person on the list.

Please do not remove this page.

RL-254-1

UCRL-9752
UC-34 Physics
TID-4500 (16th Ed)

UNIVERSITY OF CALIFORNIA
Lawrence Radiation Laboratory
Berkeley, California

Contract No. W-7405-eng-48

HYPERON PRODUCTION BY K^- MESONS INCIDENT ON HYDROGEN

William E. Humphrey
(Ph.D. Thesis)

June 12, 1961

HYPERON PRODUCTION BY K^- MESONS INCIDENT ON HYDROGEN

Contents

Abstract v

I. Introduction 1

II. Experimental Arrangement 3

III. Data Processing

A. Scanning 6

B. Event Analysis 9

IV. Analysis and Results

A. Nature of the Data

1. Events Analyzed 10

2. Corrections Applied to Data 11

B. Hyperon Decay

1. Angular Distributions for Hyperon Decay . 15

2. Hyperon Lifetimes 22

C. Hyperon Production

1. Pathlength and Energy-Dependence of Cross Sections. 29

2. Branching Ratios 32

3. Scattering-Length Parameters 32

V. Conclusions

A. Decay Rates and the $\Delta I = 1/2$ Rule 44

B. Hyperon Spins 46

C. Production Ratios for K^- Interactions At Rest . 48

D. Hyperon Production by In-Flight K^--p Interactions . 49

E. Current Extensions of the Analysis 50

Acknowledgments 51

Appendices

A. Data-Processing Programs 52

1. PANG 52

2. KICK 53

3. EXAMIN 55

4. MERGE 55
5. PATH 55
B. Maximum-Likelihood Estimate of the Number of Interactions per Momentum Interval 56
1. Formulation of the Likelihood Problem . . . 56
2. The Likelihood Solutions 61
C. Determination of K^--Nucleon Scattering Amplitudes
1. Parametrization of Low-Energy K^--p Interactions 66
2. Fitting the Data 76
References 85

HYPERON PRODUCTION BY K^- MESONS INCIDENT ON HYDROGEN

William E. Humphrey

Lawrence Radiation Laboratory
University of California
Berkeley, California

June 12, 1961

ABSTRACT

A study is presented of production and decay properties of Σ and Λ hyperons produced by K^- interactions in a hydrogen bubble chamber. Approximately 90% of the hyperons were produced by K^--p interactions at rest, and the remaining 10% were produced by K^- mesons with laboratory momentum < 275 Mev/c.

The observed hyperon decay rates from this experiment yield the hyperon mean life times:

$$\tau_{\Sigma^-} = (1.58 \pm 0.06) \times 10^{-10} \text{ sec},$$

$$\tau_{\Sigma^+} = (0.765 \pm 0.04) \times 10^{-10} \text{ sec},$$

and $$\tau_{\Lambda} = (2.69 \pm 0.11) \times 10^{-10} \text{ sec}.$$

The observed branching ratios for Σ^+ and Λ decay are

$$(\Sigma^+ \to \pi^+ + n) / [(\Sigma^+ \to \pi^+ + n) + (\Sigma^+ \to \pi^0 + p)] = 0.490 \pm 0.024,$$

and $$(\Lambda \to \pi^- + p) / [(\Lambda \to \pi^- + p) + (\Lambda \to \pi^0 + n)] = 0.643 \pm 0.016.$$

The K^--p interactions occurring at rest yield hyperon production rates in the ratio

$$\Sigma^- : \Sigma^+ : \Sigma^0 : \Lambda = 0.447 : 0.208 : 0.281 : 0.064.$$

The in-flight K^--p interactions appear to be dominated by the hyperon production process. The absorption cross section is nearly geometric for s-wave interactions throughout the observed laboratory momentum range between 75 Mev/c and 275 Mev/c. Angular distributions for the hyperon production processes are all quite consistent with isotropy.

An s-wave zero-effective-range analysis of the K^--p elastic, charge exchange and absorption processes has been carried out. The scattering lengths which best fit the data of this experiment are: $A_0 = -0.220 + 2.742i$ for the isotopic spin-0 channel, and $A_1 = 0.019 + 0.384i$ for the isotopic spin-1 channel.

I. INTRODUCTION

This work deals with the interaction of K^- mesons with protons for K^- momenta less than 275 Mev/c. At such energies, the following interactions can take place:

$$
\begin{aligned}
K^- + p &\rightarrow \Sigma^- + \pi^+, \\
&\rightarrow \Sigma^0 + \pi^0, \\
&\rightarrow \Sigma^+ + \pi^-, \\
&\rightarrow \Lambda + \pi^0, \\
&\rightarrow \Lambda + 2\pi^0; \\
\hline
&\rightarrow K^- + p, \\
&\rightarrow K^0 + n, \\
&\rightarrow \Sigma + 2\pi.
\end{aligned}
$$

K^- mesons that interact at rest can give rise to the first five interactions. The first four interactions listed have been carefully analyzed in an effort to understand the energy dependence of the hyperon production process.

The results of the analysis of the K^--proton elastic and charge-exchange scattering are presented in a separate paper.[1] They are here combined with the hyperon production analysis to obtain a description of the low-energy interactions in terms of six parameters, using the formalism of Dalitz and Tuan.[2] In connection with this parameterization, at-rest interactions of K^- mesons were assumed to occur from s-orbitals in accordance with the arguments of Day, Snow, and Sucher.[3] Other results presented in this paper are angular distributions at production and decay, and hyperon lifetimes.

A large protion of the data included in this work has been reported in the form of preliminary results presented at the 1959 Kiev Conference on High Energy Physics by Luis W. Alvarez.[4]

A recent summary of data relevent to K^- meson physics is: Freden, Gilbert and White, Phys. Rev. 118, 564 (1960). Theoretical discussions pertaining to K^- interactions are: Jackson and Wyld, Nuovo cimento X, 13, 85 (1959)., and Dalitz and Tuan, Ann. Phys., 10, 307 (1960).

II. EXPERIMENTAL ARRANGEMENT

The K^- mesons, emitted at 0 deg from a copper target in the bevatron, were guided by the bevatron field into the following beam optics (see Fig. 1):

(a) C-magnet M1 (removes momentum dispersion from beam),
(b) Single-element quadrupole Q1 (focuses in horizontal plane),
(c) Murray coaxial velocity spectrometer,
(d) Collimator C1,
(e) Double-element quadrupole Q2,
(f) Collimator C2, and
(g) Copper absorber.

The resulting beam entered the 15-inch Alvarez hydrogen bubble chamber. The chamber has a 10-in. depth and a usable region about 12 inches in diameter. It is located between a pair of coils and rests on an iron pole piece. The magnetic field in the chamber varies from about 9 to 12 kilogauss. The chamber is photographed from four lenses on a square above the chamber. The magnetic field axis and camera axes are all vertical. The expansion system is of the gas-expansion type.

Although the experimental arrangement is discussed in detail elsewhere,[5,6] the spectrometer deserves special mention, because without the enriched K beam that it produced, the experiment could not have been attempted. The spectrometer used had cylindrical symmetry about the beam direction. It consisted of a central conducting rod carrying a high current, and a coaxial cylinder around the rod which was at high potential. This configuration produces a radial electric field and an azimuthal magnetic field. In this way, a radial deflection of beam particles took place according to the particle velocity. Since the beam had already been momentum-analyzed, only particles of a given mass would have the correct velocity to be guided through the collimator C1 by the coaxial spectrometer. When the spectrometer was set to accept particles with K mass, the properties of the beam

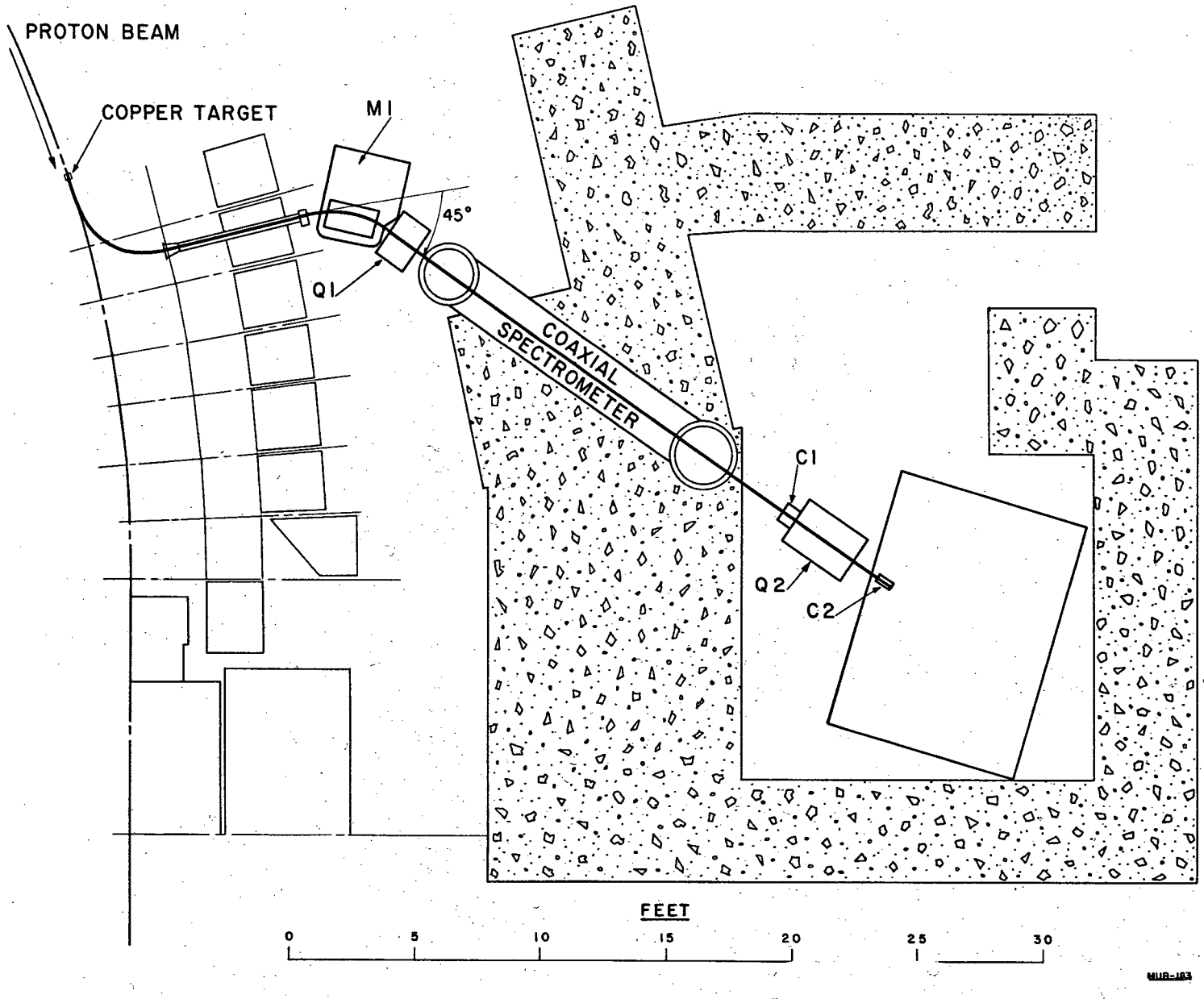

Fig. 1. Diagram of the K^--meson beam optics.

were:[6,7]

(a) Beam momentum before absorber	450 ± 23 Mev/c
(b) K^- momentum in chamber	0 to 300 Mev/c
(c) K^- in chamber per 10^{10} protons at target	1/4
(d) K^- per bubble chamber exposure	~ 1/4
(e) Background tracks per K^-	100
(f) Nature of background	~85% μ, ~15% π
(g) Background with and without spectrometer	1/700

Of the film analyzed, 38 rolls were taken with sufficient absorber to give a mean momentum of zero at the center of the chamber, and 145 rolls were taken with an absorber thickness producing a mean momentum of 180 Mev/c at the center of the chamber.

III. DATA PROCESSING

A. Scanning

A set of four stereo photographs was taken for each bubble chamber expansion. Approximately 45,000 such stereo sets were examined in accordance with the scanning method described below.

Each picture was scanned in at least two of the four views available. Detection of interactions was accomplished by temporarily masking from view all of the bubble chamber photograph except about a quarter of it at the end of the chamber through which the beam entered. From the portions of tracks visible at the beam entrance, it was possible to identify the K^- mesons by inspection on the basis of the gap density along the track, and by curvature. Background tracks with few gaps between bubbles (like the gap density of K^- tracks) were of such low momentum that the tracks could be rejected by reason of their high curvature. The number of K candidates in a photograph was recorded and then the mask was removed to reveal the full picture. Each K candidate was then traced through the picture until the K either interacted, decayed, left the chamber, or was rejected as background. Finally, the result of the track scan was recorded. Any events found during the scan of the incident tracks (mask in place) were recorded, but were not used in the analysis. The track-following method allowed event detection in such a way that the configuration of an interaction had no influence on whether or not an event was discovered by the scanner. Careful second scans show that less than 4% of the K tracks were missed, with this scanning technique.

Special emphasis in scanning was placed on the detection of neutral particles from K^-p interactions. When a K^- track terminated in the chamber volume, a search was made of all four views of the chamber to detect any pair of charged particles (these pairs form a "V" which points in the general direction of the interaction) that might represent the decay of a neutral. Since in some cases it is possible for one of the tracks forming the "V" to be very short, single tracks pointing to the end of the K^- track were also recorded.

ZN-2805

Fig. 2. The appearance of the interactions studied is well represented by this photograph of a pair of K^--p interactions yielding a Λ (upper left) and a Σ^- hyperon (low right). The ratio of K^- to background tracks is unusually high in this particular picture (roll 105, frame 160).

K^- interactions were provisionally identified at the scanning stage. This was possible because of the simple characteristic topology of the possible interactions (see Fig. 2). Sigma interactions were distinguished by the decay of the sigma within about 1 cm of the production vertex (sigmas produced by K interactions at rest have a range of about 1.1 cm). Protons from Σ^+ decay stop in the chamber about 73% of the time, and these stopping tracks could be positively identified as protons. Protons not stopping could usually be distinguished from pions by ionization. $\bar{K}^0$ decays could usually be distinguished from Λ decays by the larger opening angle of the $\bar{K}^0$ "V".

About 13% of the hyperon productions could be interpreted several ways and were recorded in appropriate classes. The principle ambiguity was between Σ^+ and Σ^-, where the Σ was very short or the Σ decayed collinearly. There were also events that could be either a short Σ^+ decaying into a proton or a short Λ. In the case of Σ production, it was also frequently possible for the scanner to select in-flight interactions from the 90% "background" of at-rest interactions. At-rest interactions produce a Σ and π collinearly, hence, noncollinear events signify in-flight interactions. An interaction at 50 Mev/c can produce a 15 deg noncollinearity between the production π and the Σ. Such a large angle is usually very easy to detect.

The events analyzed in this experiment have been restricted to a central volume of the chamber defined by certain fiducials etched in the top glass of the chamber, as seen in one of the views. The volume was chosen in such a way that events in the region were well illuminated, and particles leaving the interaction vertex were visible over a long enough distance to be measurable. At the scanning stage, events outside of the boundary were recorded, since the final selection with respect to the fiducial volume was done during the computer analysis of each event.

B. Event Analysis

Each event identified as a hyperon production in the scanning operation has gone through one or more of the following stages:

(a) Sketching—The event is carefully examined and instructions for measuring it are entered onto a card bearing a sketch of the event.

(b) Measuring—A projection microscope digitizes, in cartesian coordinates, the location of 2 to 10 points along particle tracks in the stereo photographs. These points are punched into IBM cards, together with identifying information and measurements of certain fiducials located on the bubble chamber window.

(c) Event computations—A series of IBM 704 programs are used to reconstruct the event in space and determine its kinematic parameters at interaction or decay vertices (see Appendix A).

(d) Remeasurement—Events can fail to be processed through Stage (c) for a large number of reasons ranging from measuring-machine failure to human errors. It is often necessary to reprocess events several times before obtaining acceptable measurements.

(e) Hand analysis—In the sample of events processed, there were a few events having kinematic or spatial configurations that made them difficult to analyze through the normal channels described above. In these cases, the analysis was done partially by hand and the results punched on IBM cards for handling at Stage (f). About 6% of the events were analyzed in this way.

(f) Experiment computations—At this stage all the events processed in the previous stage are examined as a whole, and the parameters of interest in the experiment are determined through a series of IBM 704 programs which use the accumulated information of both machine and hand analysis of individual events. These calculations will be described in more detail in the following section.

IV. ANALYSIS AND RESULTS

A. Nature of the Data

1. Events Analyzed

All sigmas unambiguously identified as either Σ^- production followed by decay into a π^-, or Σ^+ production followed by decay into a proton or π^+, were kinematically analyzed. There were 1488 such Σ^- and 732 such Σ^+ events in the acceptance volume for interactions. The acceptance volume also contained 204 Σ^--p interactions and 32 ambiguous Σ^+ decays that were used for corrections. There were about 314 events in the fiducial volume which were ambiguous between Σ^- and Σ^+ interpretations and about 110 events ambiguous between Σ^+ and Λ interactions. These ambiguous classes consist of events which have very short hyperons, so that the production and decay particles could not be distinguished by inspection, and such events were used only to check that the final estimate for the cross sections was consistent with the number of events in the ambiguous classes.

Of the 2194 sigma events kinematically anlayzed, only those for which the Σ hyperon had a length greater than 0.1 cm and made an angle with respect to the incident K^- of more than 20 deg were accepted in the final analysis.

All K^- interactions producing a lambda that decayed into a π^- and p, or π^- and zero-length p, were kinematically analyzed. There were 951 such events in the interaction volume. As in the analysis of the Σ hyperons, the ambiguous events (those that could be either Σ^+ or Λ production followed by decay) were not used in the analysis except as a consistency check for the final answers. Lambdas shorter than 0.1 cm were not analyzed; lambda decays outside the interaction volume were also rejected.

Only K interactions that occurred in a central volume of the bubble chamber were analyzed. This volume was defined in terms of a boundary marked by fiducials on the top glass of the chamber, as seen in one of the camera views. The volume was chosen to exclude interactions that occurred near the edge of the visible part of the bubble

chamber or in the region used in the scanning procedure to identify incoming K tracks. Tests were made in the KICK program (before the kinematic analysis) to reject events occurring outside the fiducial volume. The final tally of accepted events for the classes processed showed that 25% of the Σ^+ and Σ^- events were rejected, and 22% of the Λ events were rejected. A total number of 10,874 K tracks passed through the fiducial volume. The pathlength in the fiducial volume for all the K tracks was measured, and the momentum distribution for K mesons at the entrance plane to the fiducial volume was used to establish the amount of pathlength in the various momentum intervals. Any K pathlength, or any interaction following a visible K^--p elastic scatter, was excluded from the analysis.

Table I summarizes the number of hyperons at various stages in the analysis.

2. Corrections Applied to Data

The 0.1-cm cutoff on the hyperon length and the 20-deg K-hyperon angle cutoff served two purposes. First, it made analysis of the poorly-determined and hard-to-measure events unnecessary; and secondly, it eliminated nearly all the events in the ambiguous classes from consideration. In order to compensate for the events culled from the sample, the probability for observing each event was calculated on the basis of the selection criteria, the momentum of the hyperon, and the hyperon lifetime. For the Σ particles the acceptance probability for each event accepted was given by

$$A_\Sigma = \exp\left[-t_c/\tau\right] \frac{\cos\theta_f - \cos\theta_b}{2}$$

where t_c = time required for the Σ to travel the cutoff distance of 0.1 cm,

τ = lifetime of Σ,

θ_f = forward cutoff angle in the c.m. system, and

θ_b = backward cutoff angle in the c.m. system.

Table I

Number of events at various stages of the analysis

	Σ^-	Σ^- or Σ^+	Σ^+	Σ^+ or Λ	Λ
Events found during scan and checked	2260	419	1011	146	1229
Events in fiducial volume not preceded by Kp scatters	1547	~288[a]	709	~101[a]	871
No. of events accepted for complete analysis	1212	not analyzed	579	not analyzed	799
Final estimates (after apportioning ambiguous events) for events in fiducial volume not preceded by Kp scatters	1700	-	859	-	903

[a] These numbers were estimated from the numbers of the first row and the known rejection ratio for similar events.

The number of events before culling was then estimated from the sum

$$N_T = \sum_{i=1}^{N} \frac{1}{A_\Sigma^{\,i}}$$

where $A_\Sigma^{\,i} = A_\Sigma$ for ith culled event,

N_T = estimated number before culling, and

N = number analyzed after culling.

The ratio N_T/N was calculated separately for events in various momentum intervals, in order to allow correction of the cross section as a function of momentum. Corrections for culled Λ hyperons were carried out in much the same way as for the Σ analysis, except that an escape correction was included for each event since only Λ decays within the interaction volume were considered. As a consequence, the acceptance probability for each Λ event was computed as

$$A_\Lambda = \exp\left[-t_c/\tau\right] - \exp\left[t_e/\tau\right],$$

where t_c = time required for the Λ to travel the cutoff distance of 0.1 cm,

t_e = time required to escape through the nearest boundary plane of the interaction volume, and

τ = lifetime of Λ.

The estimate of the unculled number of events then proceeded as in the Σ analysis.

Additional corrections were found to be necessary in the hyperon analysis. Careful examination of the ambiguous Σ classes revealed that there were some Σ events that were actually longer than 0.1 cm (and should have been included in the analysis), but the Σ was hard to identify because the π decayed almost collinearly with respect to the Σ. This effect was taken into account by calculating the estimated number of Σ particles having the above properties. The number of events was calculated to be 20 Σ^+ and 30 Σ^- events, which should have been included

in the analyzed sample. The cross sections were corrected for these events by an over-all scaling factor. These additional events were predominantly short (i.e., just greater than 0.1 cm); hence, their principle effect was to modify the lifetime estimates slightly, necessitating a lifetime correction. A similar calculation was made for the ambiguous Λ class, and the additional number of Λ events which should have been analyzed was estimated to be ten. The Λ cross section was corrected for these events.

B. Hyperon Decay

1. Angular Distributions for Hyperon Decay

The cosine of the angle between the sigma and its decay pion (in the rest frame of the Σ) has been calculated for the unambiguous sigma decays. The cosine of the angle between the decay pion and the normal to the production plane was also calculated. The cosine distributions from both calculations are shown in Figs. 3 through 6. Ambiguous events between Σ^+ and Σ^- contribute a correction of about 30 events for Σ^- and 20 events for Σ^+ in the region $|\cos\theta_{\Sigma\pi}| > 0.8$. This correction is represented by the shaded regions in the figures. Not included in these figures are 26 Σ^+ events and 66 Σ^- events that were hand analyzed only at the production vertex. No particular bias is expected from these events.

The cosine of the angle between the lambda and its decay pion (in the rest frame of the Λ) is shown for direct Λ production and also for Λ's from Σ^0 decay in Fig. 7. The events for these plots were selected to include only events from K interactions having measured momenta less than 75 Mev/c, because such events represent the at-rest K interactions for which the kinematics are well enough determined to give a reliable separation between direct and indirect Λ production. Fourteen events, hand analyzed only at the production vertex, have not been included in these figures. No appreciable bias is expected from these events. There is less than 5% contamination by events which are not from K^--p at-rest interactions.

The energy distribution for Λ hyperons produced by at-rest K^--p interactions is given in Fig. 8. The $\Sigma^0 \rightarrow \gamma + \Lambda$ energy spectrum can be interpreted as a cosine distribution for the Λ with respect to the Σ^0 direction in the Σ^0 center-of-mass system, as is seen from the relation

$$E_{\Lambda KP} = -\eta P_{\Lambda\Sigma} \cos\theta + \gamma E_{\Lambda\Sigma} ,$$

where $P_{\Lambda\Sigma}$ = lambda momentum in the Σ^0 c.m. system (a constant),

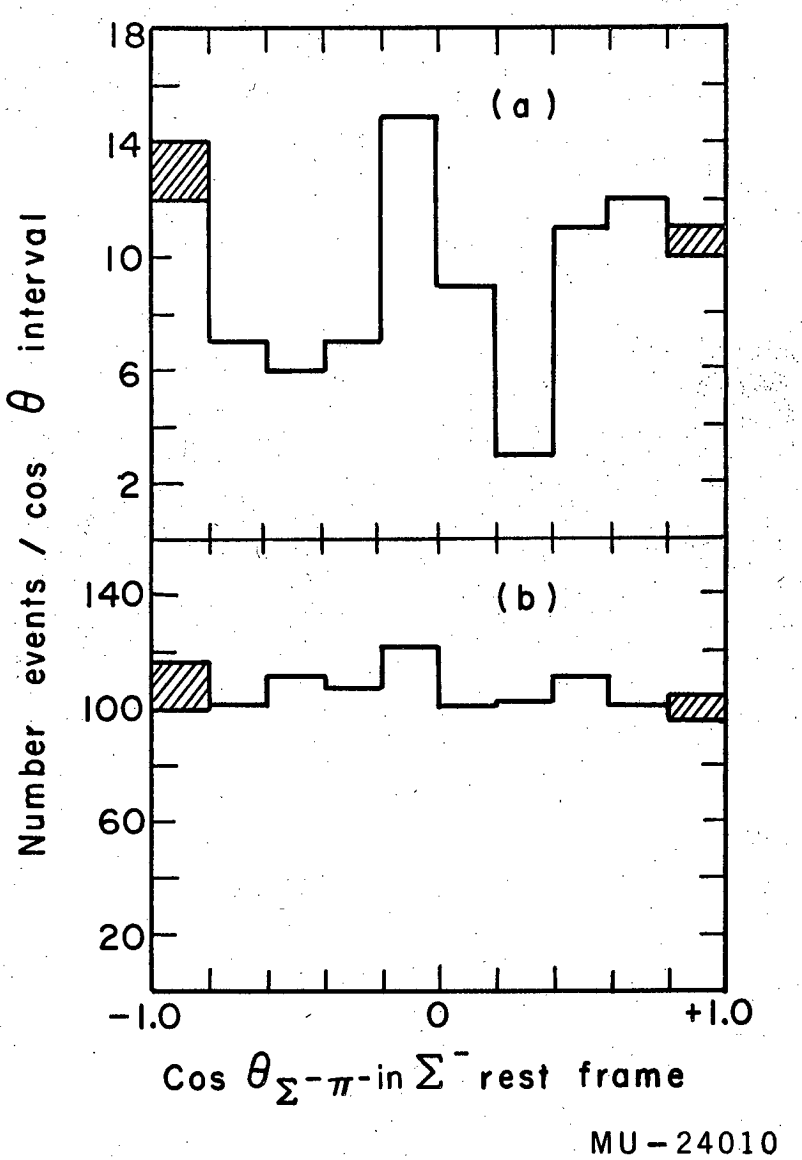

Fig. 3. Distribution of the cosine of the angle between the Σ^- hyperon and its decay pion in the rest frame of the Σ^-. The shaded areas represent corrections added to the observed distribution.

(a) In-flight K^--p interactions,
$K^- + p \rightarrow \pi^+ + \Sigma^-$, $\Sigma^- \rightarrow \pi^- + n$;

(b) At-rest K^--p interactions,
$K^- + p \rightarrow \pi^+ + \Sigma^-$, $\Sigma^- \rightarrow \pi^- + n$.

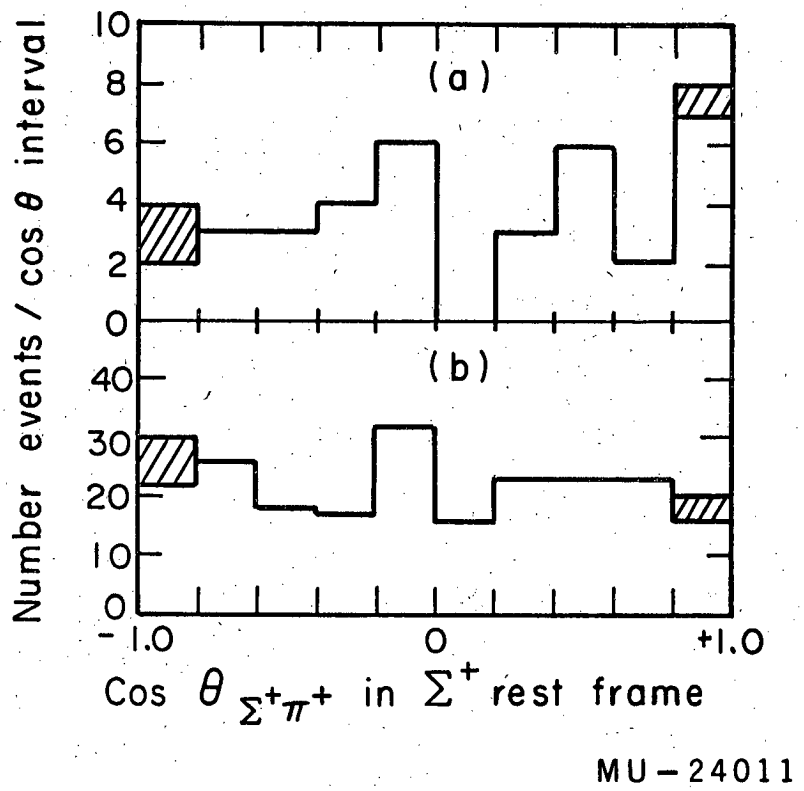

Fig. 4. Distribution of the cosine of the angle between the hyperon and its decay pion (π^+) in the rest frame of the Σ^+. The shaded areas represent corrections added to the observed distribution.

(a) In-flight K^--p interactions,
$K^- + p \rightarrow \pi^- + \Sigma^+$, $\Sigma^+ \rightarrow \pi^+ + n$;

(b) At-rest K^--p interactions,
$K^- + p \rightarrow \pi^- + \Sigma^+$, $\Sigma^+ \rightarrow \pi^+ + n$.

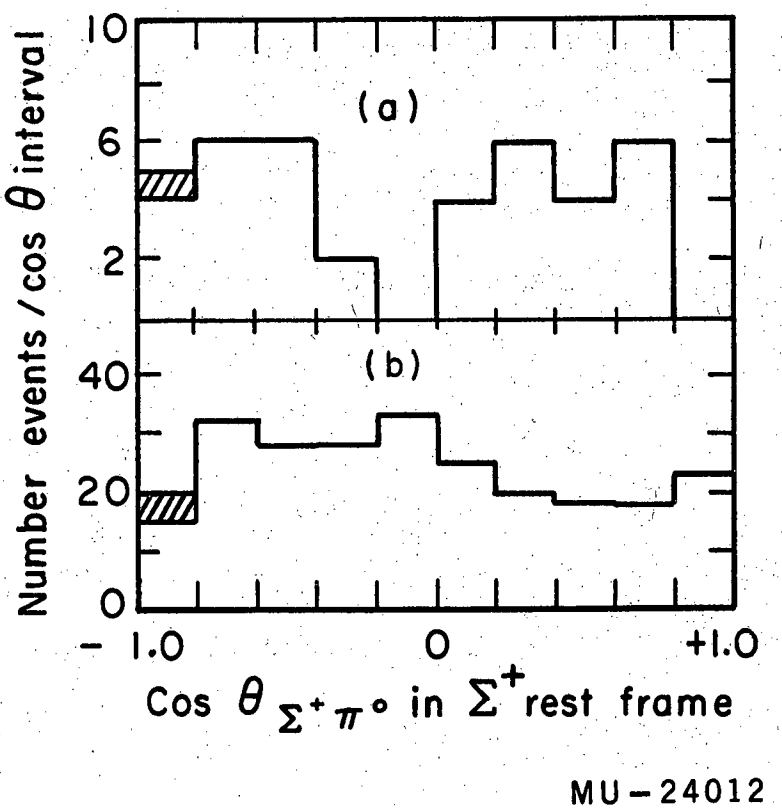

Fig. 5. Distribution of the cosine of the angle between the hyperon and its decay pion (π^0) in the rest frame of the Σ^+. The shaded areas represent corrections added to the observed distribution.

(a) In-flight K^--p interactions,
$K^- + p \rightarrow \pi^- + \Sigma^+$, $\Sigma^+ \rightarrow \pi^0 + p$;

(b) At-rest K^--p interactions,
$K^- + p \rightarrow \pi^- + \Sigma^+$, $\Sigma^+ \rightarrow \pi^0 + p$.

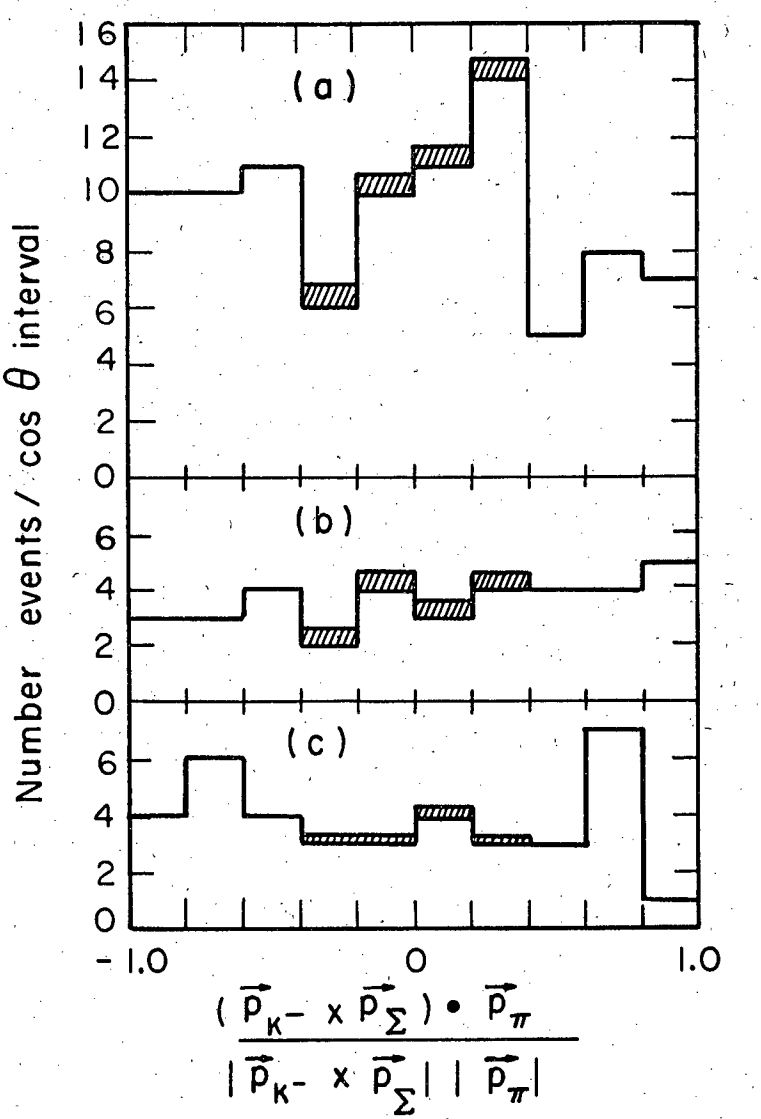

MU-24013

Fig. 6. Distribution of the cosine of the angle between the direction of motion of the decay pion and the normal to the production plane in the Σ rest frame. The shaded areas represent corrections added to the observed distribution.

(a) $K^- + p \rightarrow \pi^+ + \Sigma^-$, $\Sigma^- \rightarrow \pi^- + n$
(b) $K^- + p \rightarrow \pi^- + \Sigma^+$, $\Sigma^+ \rightarrow \pi^+ + n$
(c) $K^- + p \rightarrow \pi^- + \Sigma^+$, $\Sigma^+ \rightarrow \pi^0 + p$.

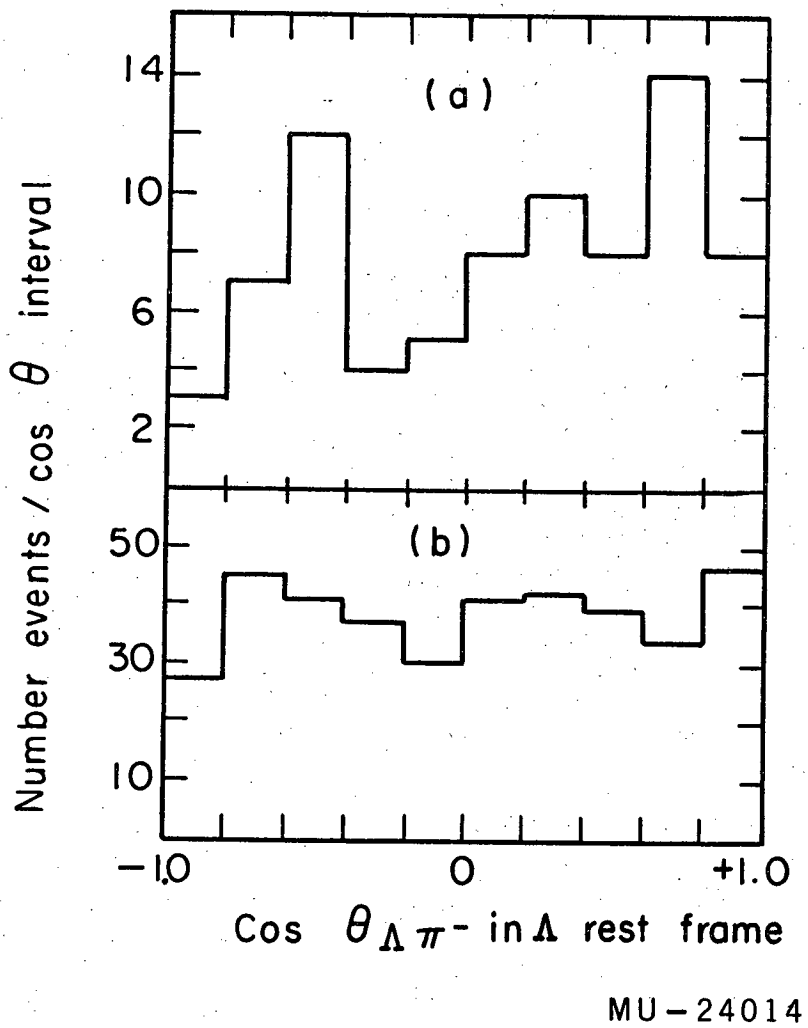

Fig. 7. Distribution of the cosine of the angle between the Λ hyperon and its decay pion (π^-) in the rest frame of the Λ.

(a) At-rest K^- interactions,
$K^- + p \rightarrow \pi^0 + \Lambda$, $\Lambda \rightarrow \pi^- + p$;

(b) At-rest K^- interactions,
$K^- + p \rightarrow \pi^0 + \Sigma^0$, $\Sigma^0 \rightarrow \gamma + \Lambda$, $\Lambda \rightarrow \pi^- + p$.

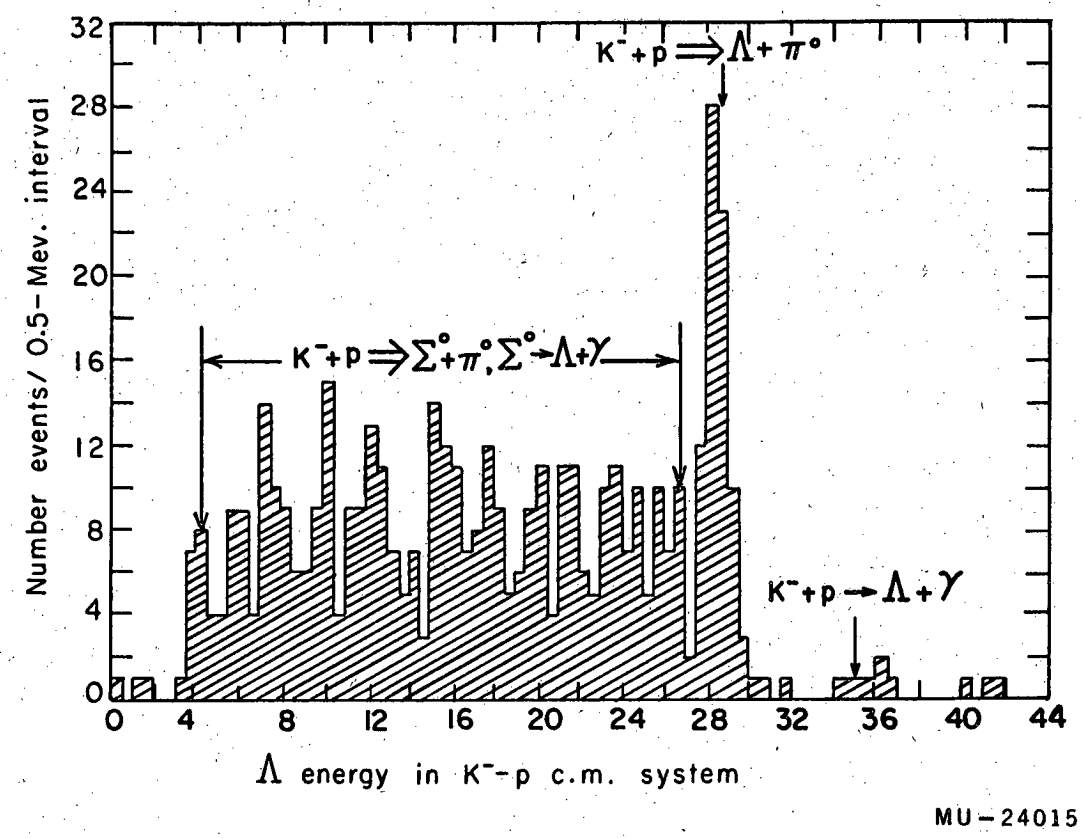

Fig. 8. The observed energy spectrum of Λ hyperons resulting from K^--p interactions at rest. The median of the energy errors is 0.36 Mev.

$E_{\Lambda\Sigma}$ = lambda energy in the Σ^0 c.m. system (a constant),

$\gamma^2 = 1 + \eta^2$, and

$\eta = \frac{P_\Sigma}{M_\Sigma}$ in the KP center-of-mass (a constant).

All of the above distributions are consistent with isotropy.

2. Hyperon Lifetimes

The lifetime of the sigmas was determined by using the maximum-likelihood method. All events with $\Sigma < 0.1$ cm long, or a Σ-K angle < 20 deg, were not included in the analysis. Only sigmas produced by K^- interactions at rest were used for lifetime estimates because the Σ momentum is well determined for these events. Sigmas that decayed in the last 0.2 cm of their range were considered to have lived a time exceeding that required to reach the 0.2 cm cutoff (this cutoff is to simplify the problem of separating Σ^- events that decay with the Σ^- at rest).

The probability for observing a given event in each of the two classes is then:

(a) $$\frac{dP_i}{dt_i} = \lambda \frac{\exp\left[-\lambda t_i\right]}{\exp\left[-\lambda t_c\right]} \text{ for } t_c < t_i < t_m, \text{ or}$$

(b) $$P_i = \frac{\exp\left[-\lambda t_m\right]}{\exp\left[-\lambda t_c\right]} \text{ for } t_i > t_m ,$$

where t_i = observed time for the ith event,

t_c = time to travel 0.1 cm from production point,

t_m = time to travel within 0.2 cm of end of range, and

λ^{-1} = mean life.

This probability is normalized to give unit probability for observing sigmas with a length exceeding 0.1 cm. This corresponds to the assertion that once the length is measured to exceed 0.1 cm, the integral of the probability for this sample must integrate to unity beyond 0.1 cm.

As a consistency check, two different likelihood functions, L_1 and L_2, were considered. First we form the product of the likelihood function for each event and take the log, to give

$$\ln L_1 = \ln \prod_{i=1}^{N} P_i = \sum_{i=1}^{N} \ln P_i = \sum_{i=1}^{N_1} \left\{ \ln\lambda - \lambda t_i + \lambda t_c \right\} + \sum_{K=1}^{N_2} \left\{ \lambda t_c - \lambda t_m \right\},$$

and the maximum of this function is located at

$$1/\lambda = 1/N_1 \left\{ \sum_{j=1}^{N_1} (t_i - t_c) + \sum_{K=1}^{N_2} (t_m - t_c) \right\} ,$$

with $\overline{\delta\lambda^2} = -(d^2 \ln L_1/d\lambda^2)^{-1} = (N_1/\lambda^2)^{-1}$, where

λ = decay rate,

N_1 = number of events with $t_c < t_i < t_m$, and

N_2 = number of events with $t_i > t_m$.

Secondly, as a consistency check, the lifetime was determined neglecting the events with $t_i > t_m$. In this case, one has

$$P_i = \frac{\lambda \exp\left[-\lambda t_i\right]}{\exp\left[-\lambda t_c\right] - \exp\left[-\lambda t_m\right]} , \quad t_c < t_i < t_m;$$

$$L_2 = \sum_{i=1}^{N_1} \left\{ \ln\lambda - \lambda t_i - \ln\left[\exp\left[-\lambda t_c\right] - \exp\left[-\lambda t_m\right]\right] \right\};$$

and one has L_2 a maximum at

$$1/\lambda = 1/N_1 \sum_{j=1}^{N_1} \left\{ t_i + \frac{t_m(\exp\left[-\lambda t_m\right]) - t_c(\exp\left[-\lambda t_c\right])}{\exp\left[-\lambda t_c\right] - \exp\left[-\lambda t_m\right]} \right\} ,$$

and $$\overline{\delta\lambda^2} = \left(N_1/\lambda^2 - \sum_{i=1}^{N_1} \frac{(t_m - t_c)^2 \exp\left[-\lambda(T_m + T_c)\right]}{\left(\exp\left[-\lambda t_c\right] - \exp\left[-\lambda t_m\right]\right)^2} \right)^{-1}$$

λ was found (using the L_2 formulation) by iteration, because the relation for λ is a transcendental one. In the case of Λ decay, where the Λ may decay outside the chamber, the second formulation (L_2) is the only applicable one. For the lambdas, t_c was defined as for the sigmas, but t_m was taken as the time for the lambda to reach the nearest boundary of the interaction volume.

As mentioned in Sec. IV-A-2 (Nature of the Data), a correction was applied to the Σ lifetimes to account for events in the ambiguous catagories which really should have been included in the lifetime calculation, because their length exceeded 0.1 cm. The number of such events was estimated as 20 for Σ^+, and 30 for Σ^-. The model used to calculate the number of events was also used to calculate the amount of time they contribute to the lifetime calculation, and these numbers were inserted in the previous equations to obtain the corrected lifetimes. A small correction was applied to the Σ^- lifetime to account for the Σ^--p interactions in flight. The corrections decreased both the Σ^+ and Σ^- lifetime by 0.01×10^{-10} sec. The results of the lifetime calculations are shown in Table II. The best lifetime estimates from this experiment are plotted against the observed decay frequencies in Figs. 9 through 11.

The branching ratio between neutral and charged Λ decay was determined by counting the number of K tracks that stopped in the fiducial volume of the chamber with no visible hyperon decay. This number was corrected for neutral $\overline{K}^0$ decays and Λ decays outside of the chamber (a correction of 54 events). The ratio obtained was

$$\frac{\Lambda \text{ charged}}{\Lambda \text{ total}} = \frac{903}{1405} = 0.64 \pm 0.01.$$

The branching ratio between neutron and proton decay modes of Σ^+ hyperons was found to be

$$\frac{\Sigma^+ \text{ neutron}}{\Sigma^+ \text{ total}} = \frac{308}{628} = 0.49 \pm 0.02.$$

As a consistency check, two different likelihood functions, L_1 and L_2, were considered. First we form the product of the likelihood function for each event and take the log, to give

$$\ln L_1 = \ln \prod_{i=1}^{N} P_i = \sum_{i=1}^{N} \ln P_i = \sum_{i=1}^{N_1} \left\{ \ln\lambda - \lambda t_i + \lambda t_c \right\} + \sum_{K=1}^{N_2} \left\{ \lambda t_c - \lambda t_m \right\},$$

and the maximum of this function is located at

$$1/\lambda = 1/N_1 \left\{ \sum_{j=1}^{N_1} (t_i - t_c) + \sum_{K=1}^{N_2} (t_m - t_c) \right\},$$

with $\overline{\delta\lambda^2} = -(d^2 \ln L_1/d\lambda^2)^{-1} = (N_1/\lambda^2)^{-1}$, where

λ = decay rate,

N_1 = number of events with $t_c < t_i < t_m$, and

N_2 = number of events with $t_i > t_m$.

Secondly, as a consistency check, the lifetime was determined neglecting the events with $t_i > t_m$. In this case, one has

$$P_i = \frac{\lambda \exp\left[-\lambda t_i\right]}{\exp\left[-\lambda t_c\right] - \exp\left[-\lambda t_m\right]}, \quad t_c < t_i < t_m;$$

$$L_2 = \sum_{i=1}^{N_1} \left\{ \ln\lambda - \lambda t_i - \ln\left[\exp\left[-\lambda t_c\right] - \exp\left[-\lambda t_m\right]\right] \right\};$$

and one has L_2 a maximum at

$$1/\lambda = 1/N_1 \sum_{j=1}^{N_1} \left\{ t_i + \frac{t_m(\exp\left[-\lambda t_m\right]) - t_c(\exp\left[-\lambda t_c\right])}{\exp\left[-\lambda t_c\right] - \exp\left[-\lambda t_m\right]} \right\},$$

and $$\overline{\delta\lambda^2} = \left(N_1/\lambda^2 - \sum_{i=1}^{N_1} \frac{(t_m - t_c)^2 \exp\left[-\lambda(T_m + T_c)\right]}{\left(\exp\left[-\lambda t_c\right] - \exp\left[-\lambda t_m\right]\right)^2} \right)^{-1}$$

λ was found (using the L_2 formulation) by iteration, because the relation for λ is a transcendental one. In the case of Λ decay, where the Λ may decay outside the chamber, the second formulation (L_2) is the only applicable one. For the lambdas, t_c was defined as for the sigmas, but t_m was taken as the time for the lambda to reach the nearest boundary of the interaction volume.

As mentioned in Sec. IV-A-2 (Nature of the Data), a correction was applied to the Σ lifetimes to account for events in the ambiguous catagories which really should have been included in the lifetime calculation, because their length exceeded 0.1 cm. The number of such events was estimated as 20 for Σ^+, and 30 for Σ^-. The model used to calculate the number of events was also used to calculate the amount of time they contribute to the lifetime calculation, and these numbers were inserted in the previous equations to obtain the corrected lifetimes. A small correction was applied to the Σ^- lifetime to account for the Σ^--p interactions in flight. The corrections decreased both the Σ^+ and Σ^- lifetime by 0.01×10^{-10} sec. The results of the lifetime calculations are shown in Table II. The best lifetime estimates from this experiment are plotted against the observed decay frequencies in Figs. 9 through 11.

The branching ratio between neutral and charged Λ decay was determined by counting the number of K tracks that stopped in the fiducial volume of the chamber with no visible hyperon decay. This number was corrected for neutral $\overline{K}^0$ decays and Λ decays outside of the chamber (a correction of 54 events). The ratio obtained was

$$\frac{\Lambda \text{ charged}}{\Lambda \text{ total}} = \frac{903}{1405} = 0.64 \pm 0.01.$$

The branching ratio between neutron and proton decay modes of Σ^+ hyperons was found to be

$$\frac{\Sigma^+ \text{ neutron}}{\Sigma^+ \text{ total}} = \frac{308}{628} = 0.49 \pm 0.02.$$

There were 17 events ambiguous between proton and neutron decay modes, divided equally between the two modes for the purpose of calculating the branching ratio. The error in the branching ratio includes a contribution for these ambiguous events.

These branching ratios are in excellent agreement with the $\Delta I = 1/2$ rule.[8]

Table II

Summary of lifetime calculations

Times (10^{-10} sec units)	Σ^-	Σ^+	Λ
t_c	0.226	0.216	event-dependent
t_m	2.553	3.024	event-dependent
N_1	940	445	799
N_2	268	11	———
L_1 lifetime calculation	1.58 ± 0.06	0.765 ± 0.04	———
L_2 lifetime calculation	1.63 ± 0.13	0.755 ± 0.05	2.69 ± 0.11
Best lifetime estimate	1.58 ± 0.06	0.765 ± 0.04	2.69 ± 0.11

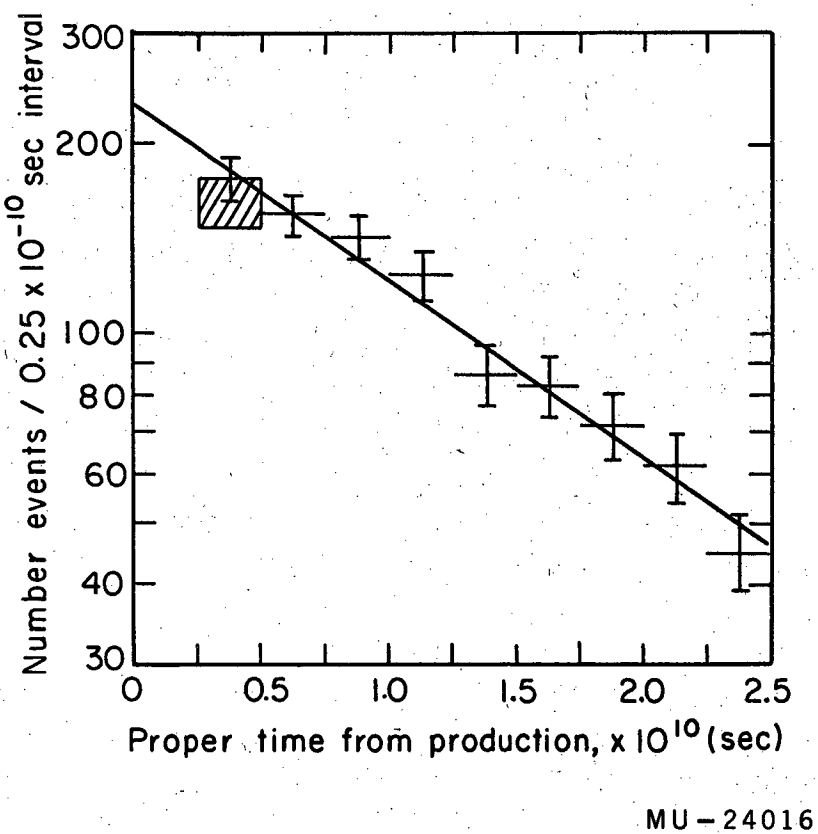

Fig. 9. Number of Σ^- decays plotted as a function of the proper time from the time of production. The shaded area represents a correction added to the observed distribution. A line having the slope of the maximum-likelihood lifetime estimate ($\tau_{\Sigma^-} = 1.58 \times 10^{-10}$ sec) is superimposed on the data.

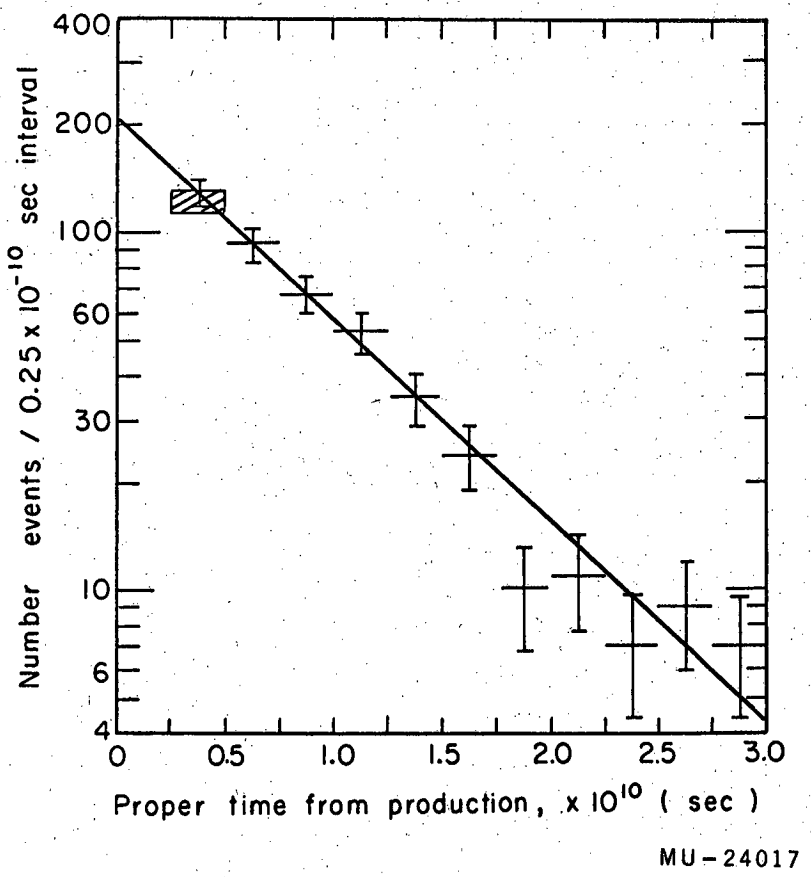

Fig. 10. Number of Σ^+ decays plotted as a function of the proper time from the time of production. The shaded area represents a correction added to the observed distribution. A line having the slope of the maximum-likelihood lifetime estimate ($\tau_{\Sigma^+} = 0.765 \times 10^{-10}$ sec) is superimposed on the data.

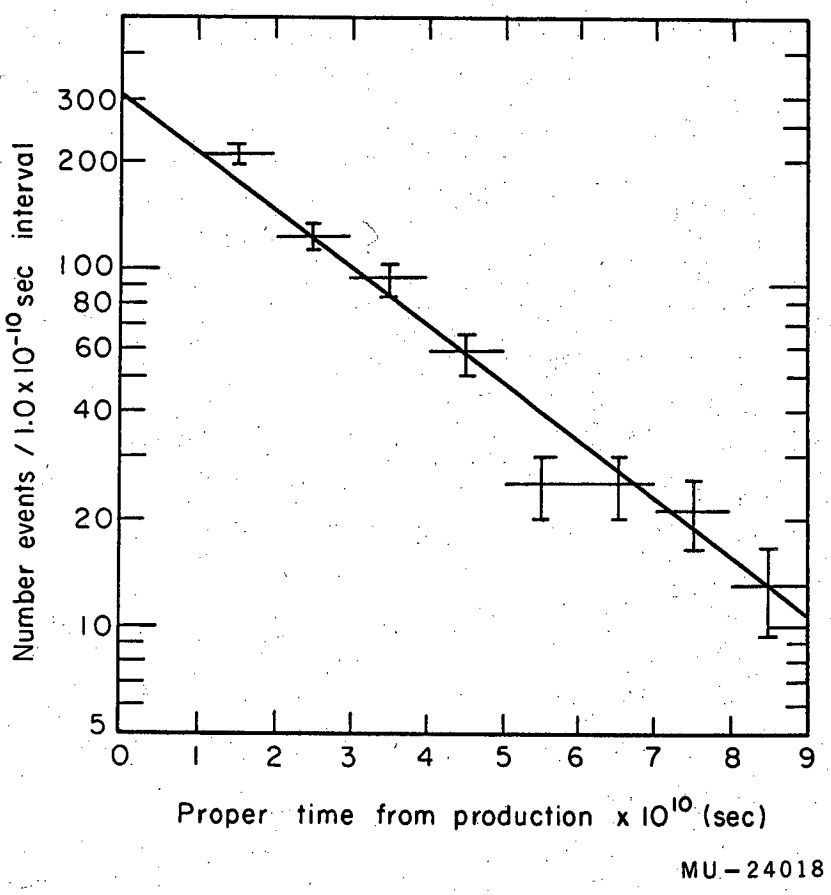

Fig. 11. Number of Λ decays plotted as a function of the proper time from the time of production. A line having the slope of the maximum-likelihood lifetime estimate (2.69×10^{-10} sec) is superimposed on the data.

C. Hyperon Production

1. Pathlength and Energy-Dependence of Cross Sections

The energy spread of the beam entering the bubble chamber was such that K^- interactions occurred at momenta ranging from about 300 Mev/c to 0 Mev/c. About 90% of the hyperon interactions occurred at rest. Although the energy spread allows investigation of the entire low-energy region as a whole, there are also complications connected with the wide range of interaction energies. The cross section is defined in terms of the relation

$$n = \sigma \ell \{\rho N_0/A\},$$

where $\rho N_0/A$ = number of protons per unit volume,

ρ = density of hydrogen liquid (0.0586 g/cm^3),[9]

N_0 = Avogadro's number,

A_0 = atomic weight of hydrogen,

σ = cross section,

ℓ = length of observed K^- track length, and

n = number of interactions observed.

However, since the cross section and the observed pathlength vary as a function of the momentum interval being considered, two basic tasks must be completed before the cross section can be determined in several momentum intervals.

The first task is the estimation of the pathlength observed in the various momentum intervals from 0 to 300 Mev/c. All the K tracks that entered the interaction volume were measured, and the length of path and momentum at an entrance plane were calculated.[1] In the case of the interactions that were fitted, the momentum at the entrance plane was very well known from the kinematic fit of the interaction. However, the rest of the K tracks depended for their momentum measurement on the observed curvature of the track in the magnetic field of the bubble chamber. These curvature measurements typically had 6% to 10% uncertainties.

The momentum distribution at the entrance plane to the interaction volume has a predominance of tracks in a relatively narrow region of the momentum spectrum considered (about 200 to 250 Mev/c). As a consequence, the momentum measurement errors tend to smear out the peak in the momentum distribution. It was necessary to recover the original distribution by unfolding the observed distribution. To do this, the following matrix relationship was used:

$$L_0 = (T)L_T,$$

where L_T = vector representing the true number of tracks in each of 12 momentum intervals at the entrance plane,

L_0 = vector representing the observed number of tracks in each of 12 momentum intervals at the entrance plane,

T_{ji} = represents a matrix element indicating the percentage of events in the ith true interval that would be observed in the jth observed interval, on the basis of the typical error for events in the ith interval.

After solving for L_T, a range-momentum table was used to establish how much pathlength was contributed in the various momentum intervals by tracks distributed according to the vector L_T. This unfolding procedure was applied to events from each of four thicknesses of copper absorber used in this experiment, and these pathlengths were accumulated, along with the pathlength for the interactions, to give the pathlength per momentum interval displayed in Fig. 12. This pathlength includes only K track length in the interaction volume not preceded by a visible K-P scatter.

The second task, before the cross sections can be computed, is to estimate the true number of interactions in the various momentum intervals on the basis of the observed momentum distribution. This procedure is complicated by the fact that the low-energy interactions are plagued by a "background" of stopping interactions. Moreover, the precision with which the momentum of the K is determined varies over a factor of 10, according to the configuration of the individual events.

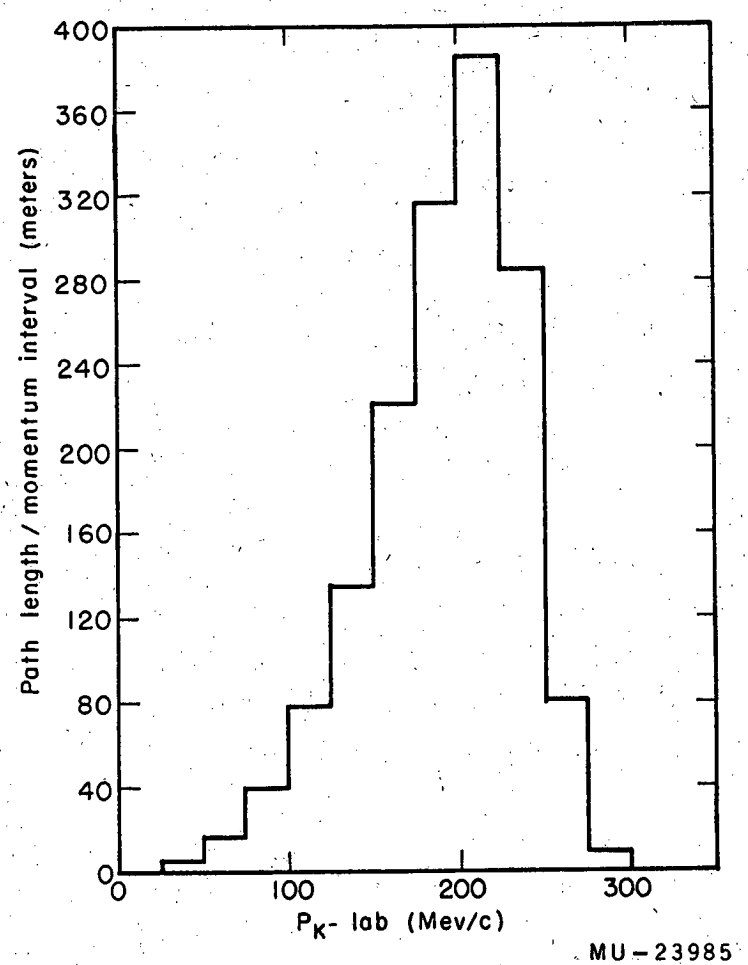

Fig. 12. Pathlength distribution plotted as a function of K^- momentum in the laboratory.

Therefore, a maximum-likelihood estimate was made for the true momentum distribution using the observed error for each event (see Appendix B).

Errors were propagated to the cross section estimates from both the matrix-inversion technique and the maximum-likelihood method. The estimates for the cross sections are shown in Figs. 13 and 14 and summarized in Tables III, IV, and V. For each charged Σ event giving an in-flight fit, the laboratory momentum and c.m. cosine have been plotted on a scatter diagram (Figs. 15 and 16).

2. Branching Ratios

The branching ratio between Σ^- and Σ^+ production falls out as a consequence of the cross-section analysis. The measurement of the Λ to Σ^0 ratio is not so simple. The most reliable value is the one obtained for Λ production by K interactions at rest, where the separation between direct and indirect Λ's can almost be done by inspection (see Fig. 8.). Four of the events, with an energy near 35 Mev, are interpreted as $K^- + p \rightarrow \gamma + \Lambda$, which implies a branching ratio for this process of about 0.8% of the total Λ production. There is a cluster of events at 40 Mev, two of which have energies that are well-determined and within errors of each other. These events are interpreted as in-flight K interactions. The $\Lambda/(\Sigma^0 + \Lambda)$ separation was done by the maximum-likelihood method for K interactions, both at-rest and in-flight. A plot of the likelihood function for the at-rest events is shown in Fig. 17, and the in-flight ratios are indicated in Fig. 18. Seven events with energies in excess of 3 standard deviations from either the Λ or the Σ^0 spectrum were not included in the likelihood calculations. The production branching ratios are summarized in Table VI.

3. Scattering-Length Parameters

The theory of low-energy (s-wave) K^--p interactions presented by Dalitz and Tuan has been used to fit all the interaction processes observed in this experiment, including the K^--p elastic and charge-exchange cross sections.[2] Two distinct solutions were found using this formulation, and for each, the optimum value of six parameters used in

Table III

Momentum dependence of the Σ^- cross section.

K^- Lab Momentum Interval (Mev/c)	Experimental Cross Section Estimate	Variance matrix for estimate of cross section								
		50-75	75-100	100-125	125-150	150-175	175-200	200-225	225-250	250-275
50-75	217.5	9499.8	The symmetric elements of the variance matrix							
75-100	110.3	-1088.6	1774.2	$(\overline{\delta\sigma_i\,\delta\sigma_j})$ have not been duplicated.						
100-125	42.0	32.7	-121.9	416.7						
125-150	48.3	2.0	-1.2	-95.4	226.8					
150-175	10.7	-0.1	-0.3	6.5	-20.7	43.3				
175-200	35.7	-0.6	-0.2	-0.5	1.5	-11.6	63.4			
200-225	15.8	-0.3	-0.2	0.0	-0.3	1.7	-12.7	32.3		
225-250	10.4	-0.2	-0.1	-0.1	0.0	-0.4	3.2	-10.7	30.9	
250-275	17.3	-0.5	-0.2	-0.1	-0.2	0.2	-1.9	6.0	-22.0	138.8

Table IV

Momentum dependence of the Σ^+ cross section.

K^- Lab Momentum Interval (Mev/c)	Experimental Cross Section Estimate	Variance matrix for estimate of cross section							
		75-100	100-125	125-150	150-175	175-200	200-225	225-250	250-275
75-100	27.8	754.0	The symmetric elements of the variance matrix $(\overline{\delta\sigma_i \delta\sigma_j})$ have not been duplicated.						
100-125	75.8	-202.2	739.6						
125-150	20.8	27.7	-159.0	237.6					
150-175	39.1	-4.9	17.0	-56.5	122.2				
175-200	20.6	0.4	-3.0	4.8	-18.3	55.4			
200-225	18.2	-0.1	0.2	-0.7	2.7	-12.0	33.6		
225-250	21.3	-0.1	-0.2	0.1	-0.6	1.7	-9.1	46.8	
250-275	15.3	-0.1	-0.1	-0.1	0.1	-0.5	3.1	-22.9	140.9

Table V

Momentum dependence of the $(\Sigma^0 + \Lambda)$ cross section

K^- Lab Momentum Interval (Mev/c)	Experimental Cross Section Estimate	Variance matrix for estimate of cross section				
		125-150	150-175	175-200	200-225	225-250
125-150	154.7	32864.2	The symmetric elements of the variance matrix $(\overline{\delta\sigma_i \, \delta\sigma_j})$ have not been duplicated			
150-175	86.7	-18324.2	12174.1			
175-200	11.2	5981.4	-4512.0	2262.8		
200-225	34.6	-1737.6	1443.2	-920.1	557.2	
225-250	5.4	626.4	-534.5	361.5	-245.2	161.5

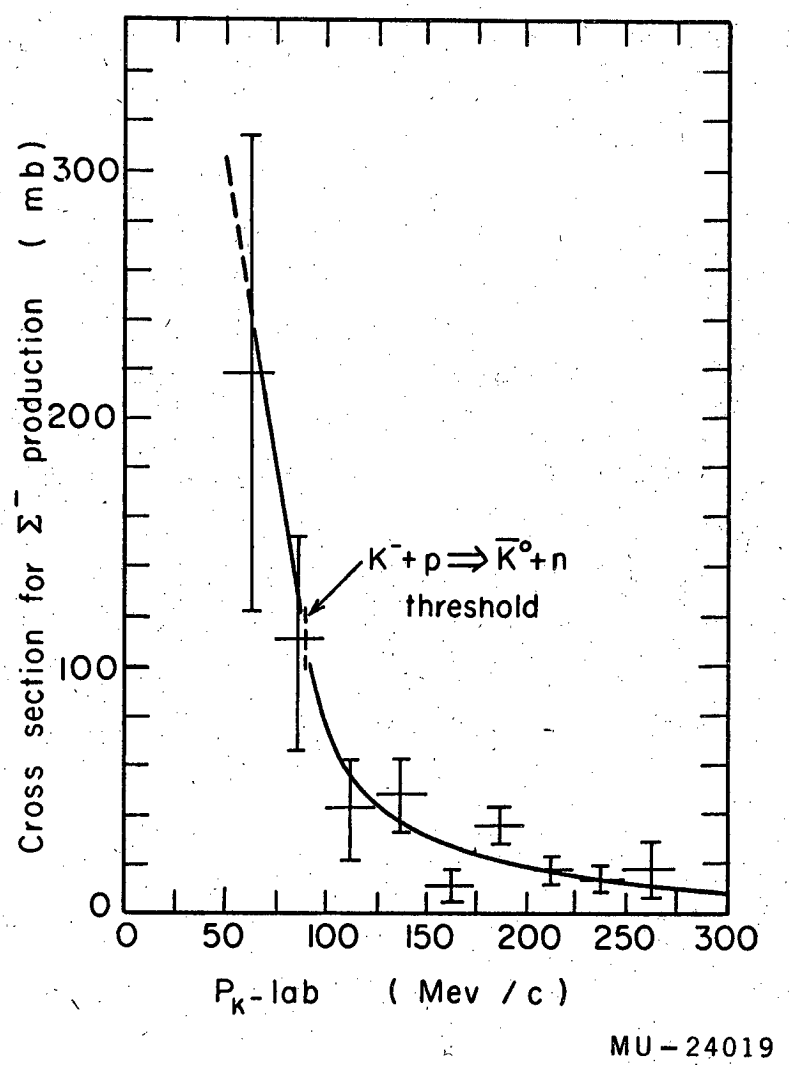

Fig. 13. Cross section for production of Σ^- hyperons presented as a function of the K^- momentum in the laboratory. The solid curve represents the theoretical prediction for the better of the two scattering length solutions (solution I).

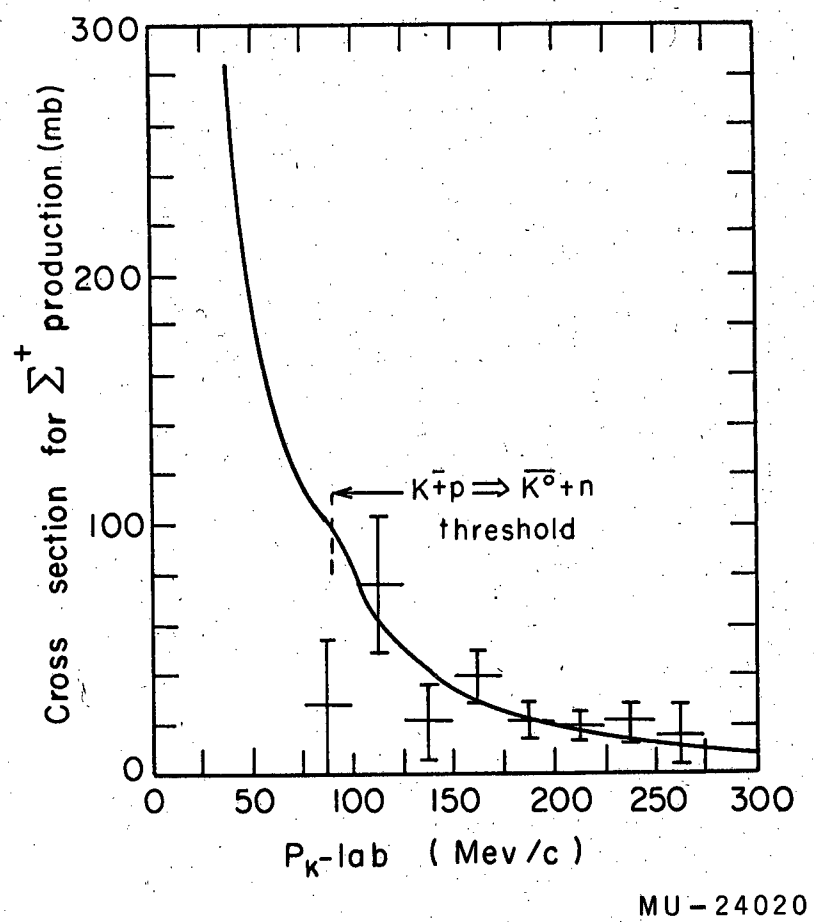

Fig. 14. Cross section for production of Σ^+ hyperons presented as a function of the K^- laboratory momentum. The solid curve represents the theoretical prediction for the better of the two scattering length solutions (solution I).

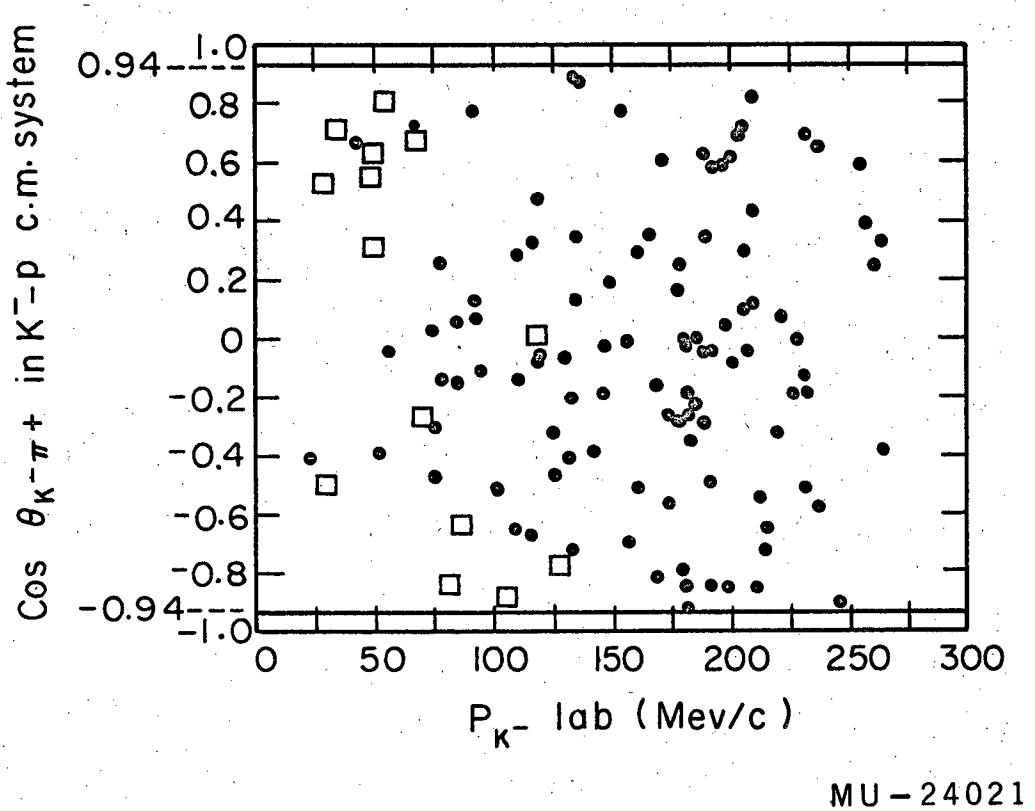

Fig. 15. Each Σ^- produced by an in-flight K^--p interaction is represented by a point whose coordinates are the K^- production angle in the K^--p c.m. system, and the K^- laboratory momentum. Events that are not in-flight by inspection are indicated by a square (these events have fitted momenta which are at least three standard deviations from stopping).

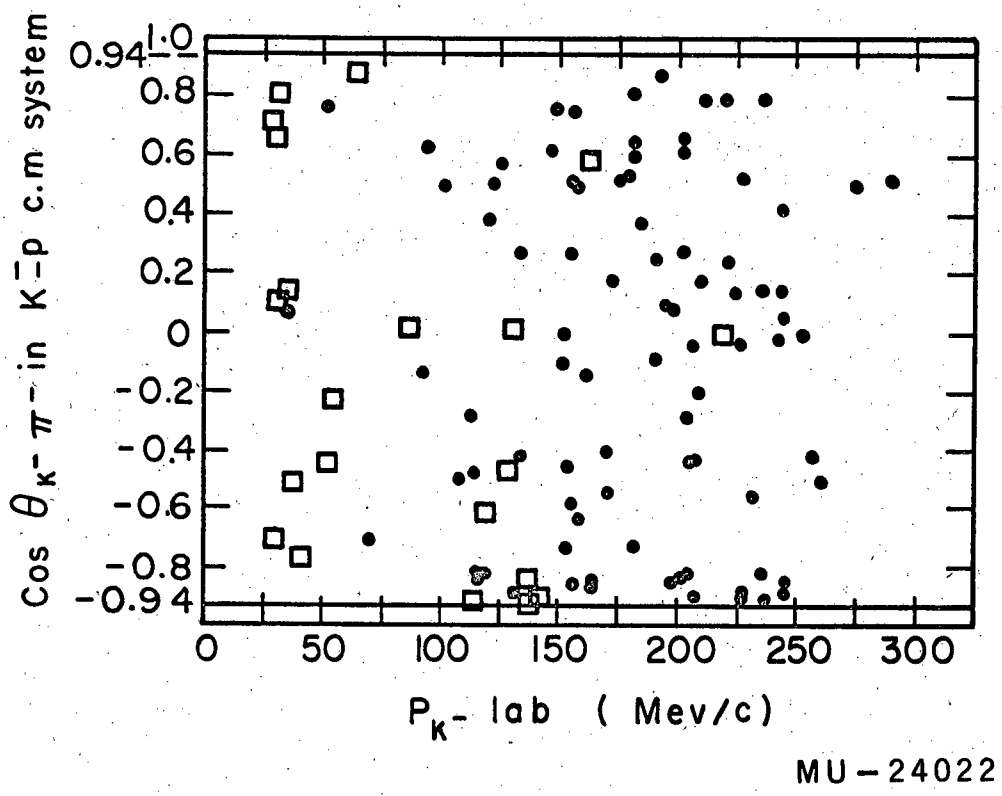

Fig. 16. Each Σ^+ produced by an in-flight K^--p interaction is represented by a point whose coordinates are the production angle in the K^--p c.m. system, and the K^- laboratory momentum. Events that are not in-flight by inspection are indicated by a square (these events have fitted momenta which are at least three standard deviations from stopping).

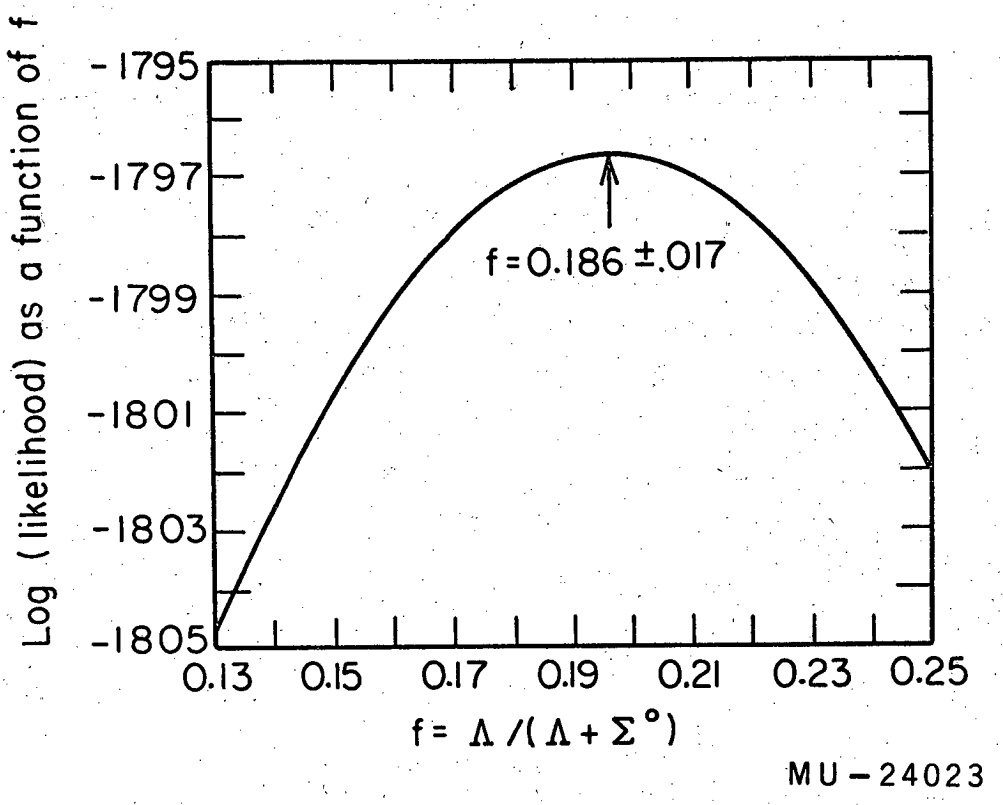

Fig. 17. Log of the likelihood plotted as a function of the branching ratio $\Lambda/(\Lambda+\Sigma^0)$.

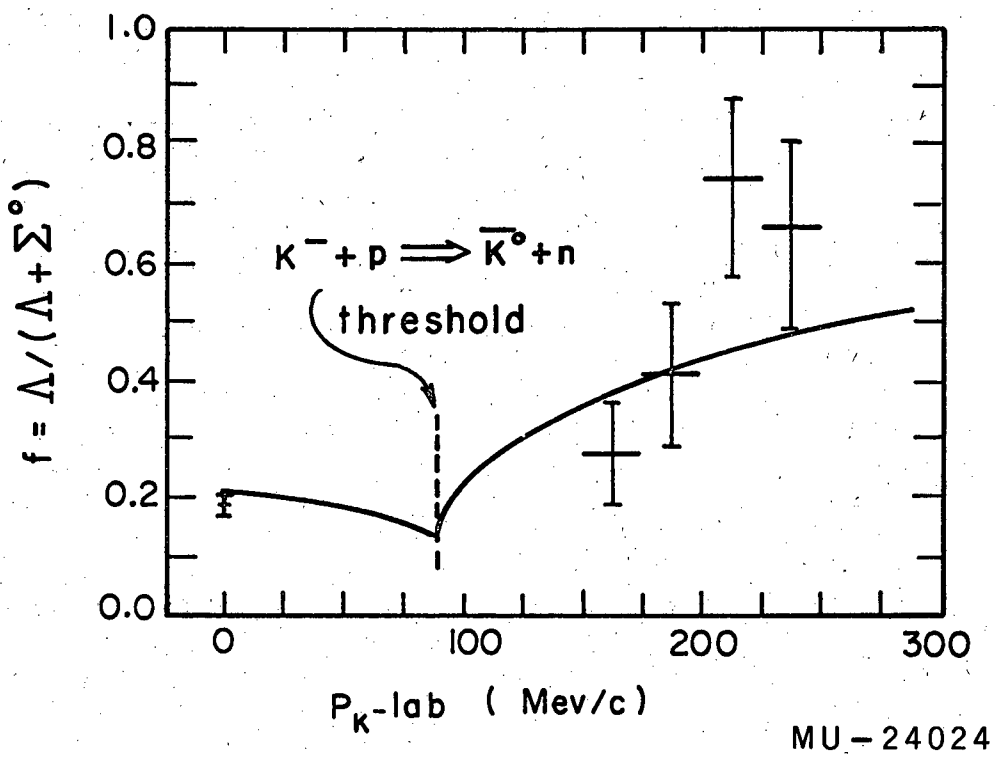

Fig. 18. Branching ratio $\Lambda/(\Lambda+\Sigma^0)$ presented as a function of the K^- momentum in the laboratory. The solid curve represents the theoretical prediction for the better of the two scattering length solutions (solution I).

Table VI

Estimated number of events in acceptance volume as a function of laboratory momentum

K^- Lab Momentum Interval (Mev/c)	Σ^-		Σ^+		$\Sigma^0 + \Lambda$		
	Number Analyzed	Estimated Number	Number Analyzed	Estimated Number	Number Analyzed	Estimated Number	Neutral Decays Included
at rest	1101	1553.3	477	721.7	471	771.2	1199.8
50-75	7	12.3	6	--	--	--	--
75-100	14	15.2	5	3.8	60	--	--
100-125	12	11.5	12	20.8	123	--	--
125-150	14	23.1	11	9.9	67	47.6	74.0
150-175	10	8.3	18	30.3	34	43.2	67.2
175-200	24	39.5	12	22.8	22	7.9	12.4
200-225	16	21.3	18	24.6	10	30.1	46.8
225-250	9	10.4	15	21.3	11	3.5	5.4
250-275	5	4.9	4	4.3	0	0.0	0.0
275-300	0	--	1	--	0	--	--

the theory have been determined by minimizing the difference between theoretical and observed cross sections (using the least-squares method). The χ^2 function included cross sections in 57 momentum and angle intervals, and 7 branching ratios (see Appendix C). The solutions and their χ^2 are listed in Table XI.

V. CONCLUSIONS

A. Decay Rates and the $\Delta I=1/2$ Rule

The $\Delta I=1/2$ rule makes a definite prediction for the ratio of the decay matrix elements for $\Lambda \to \pi^0 + n$ and $\pi^- + p$ decay.[8] The prediction is:

$$\frac{s_-^2 + p_-^2}{(s_-^2 + p_-^2) + (s_0^2 + p_0^2)} = 2/3 ,$$

where s_- and p_- are s- and p-wave amplitudes for the $\pi^- + p$ decay mode, and s_0 and p_0 are s- and p-wave amplitudes for the $\pi^0 + n$ decay mode. The experimental branching ratio from this experiment is

$$\frac{(\pi^- + p)}{(\pi^0 + n) + (\pi^- + p)} = 0.643 \pm 0.016,$$

which, after taking account of phase space for the two decay modes, yields the value

$$\frac{s_-^2 + p_-^2}{(s_-^2 + p_-^2) + (s_0^2 + p_0^2)} = 0.650 \pm 0.016.$$

Another interesting (but less constraining) prediction following from the $\Delta I = 1/2$ rule concerns the relative size of the amplitudes for the three decay modes of charged Σ hyperons. If the s and p amplitudes for a single decay mode are represented as a two-dimensional vector, then the $\Delta I = 1/2$ rule predicts the following vector relationship:[8]

$$\sqrt{2}\,\vec{A}_0 + \vec{A}_+ = \vec{A}_- ,$$

where $\vec{A}_0$ corresponds to $\Sigma^+ \to \pi^0 + p$,

$\vec{A}_+$ corresponds to $\Sigma^+ \to \pi^+ + n$, and

$\vec{A}_-$ corresponds to $\Sigma^- \rightarrow \pi^- + n$.

The decay rates for the three decay modes have been determined in this experiment to be:

$$R_0 = (0.666 \pm 0.047) \times 10^{10}/\text{sec},$$

$$R_+ = (0.641 \pm 0.046) \times 10^{10}/\text{sec}, \text{ and}$$

$$R_- = (0.634 \pm 0.025) \times 10^{10}/\text{sec}.$$

Therefore, the amplitudes (including the phase space correction) have relative sizes

$$|A_0| = 0.544 \pm 0.019 ,$$

$$|A_+| = 0.540 \pm 0.019 , \text{ and}$$

$$|A_-| = 0.527 \pm 0.010 .$$

The resulting vector triangle has an angle between $\vec{A}_-$ and $\vec{A}_+$ of 92.4 ±4.8 deg. Measurements of the decay assymmetries for Σ^+ decay reveal that the vector $\vec{A}_0$ must have appreciable components of both s- and p-wave amplitudes, while $\vec{A}_+$ must be an almost pure s or p wave.[10] Σ^- decay suggests that $\vec{A}_-$ is also almost pure s or p wave.[11] Hence the vector triangle has the remarkable property that it appears to be nearly a right triangle with its legs about 1 deg from the s and p axes. Theoretical significance has been attached to this striking alignment of the triangle in a paper by A. Pais,[12] in which the suggestion is made that the weak as well as the strong interactions might be coupled through a doublet approximation model of the elementary particles.

The experimental results are certainly very consistent with the predictions of the $\Delta I=1/2$ rule; however, only the magnitudes of the decay amplitudes are observable in this experiment and not the phases. It has been pointed out that appropriate mixtures of $\Delta I=1/2$ and $\Delta I=3/2$ can give rise to the same physical consequences as the $\Delta I=1/2$ rule, but with certain phases shifted by 180 deg.[13]

B. Hyperon Spins

The spin of the hyperons has been determined by previous experiments;[14, 15, 16] however, further evidence is available from this experiment, subject to two assumptions. First, it is assumed that the K meson has spin zero.[15] Secondly, K interactions that occur at rest are assumed to take place from s orbits in accordance with the calculations of Day, Snow, and Sucher.[3] If we make these assumptions, it is clear that the angular momentum of the initial state is $J = 1/2$. Therefore, the maximum angular momentum component along the direction of the Σ can not exceed 1/2, by conservation of the component of J projected along the Σ. This means that if the Σ hyperon spin is greater than 1/2, certain spin states with angular momentum component in excess of 1/2 along the Σ direction are forbidden. As a result, only spin 1/2 can give an isotropic distribution.[16] Spin 3/2 gives a distribution of the form $1 + 3 \cos^2\theta$.

The Σ^+ and Σ^- decay distributions for K^- interactions at rest have been fitted to distributions of the form $N = a_1 + a_2 \cos\theta + a_3 \cos^2\theta$. The results shown in Table VII provide strong evidence that both Σ^- and Σ^+ are spin 1/2 particles. The same argument applies to the directly produced Λ hyperons; the result recorded in Table VII strongly indicates isotropy, hence spin 1/2 for the Λ.

The Σ^0 spin can be established with certainty under the rather tenuous assumption of odd $\Sigma^0 - \Lambda$ parity.[17] In this case, it is possible to show that the $\Sigma^0 - \Lambda$ distribution is isotropic for spin 1/2 and is $(1 + 0.6 \cos^2\theta)$ for spin 3/2. Again, isotropy is highly favored, as can be seen from Table VII.

Table VII

Decay angular distributions

Decay mode	Angle	Interval Widths	$N = a_1 + a_2 \cos\theta + a_3 \cos^2\theta$				Degrees of freedom	χ^2
			a_1	a_2	a_3	a_3/a_1		
$\Sigma^- \to \pi^- + n$ (Fig. 3b)	$\Sigma^- - \pi$	0.2	108.6 ± 5.0	-4.2 ± 5.7	-2.3 ± 11.3	-0.02 ± 0.10	7	3.6
$\Sigma^+ \to \pi^+ + n$ (Fig. 4b)	$\Sigma^+ - \pi$	0.2	20.0 ± 2.3	-2.7 ± 2.6	6.5 ± 5.2	0.33 ± 0.29	7	13.6
$\Sigma^+ \to \pi^0 + p$ (Fig. 5b)	$\Sigma^+ - \pi$	0.2	26.6 ± 2.4	-4.4 ± 2.7	-6.6 ± 5.4	-0.25 ± 0.19	7	7.8
$\Sigma^+ \to \begin{cases} \pi^+ + n \\ \pi^0 + p \end{cases}$	$\Sigma^+ - \pi$	0.2	48.0 ± 3.3	-6.9 ± 3.8	-2.4 ± 7.5	-0.05 ± 0.16	7	9.1
$\Lambda \to \pi^- + p$ Direct (Fig. 7a)	$\Lambda - \pi$	0.2	8.1 ± 1.3	2.9 ± 1.6	-0.6 ± 3.1	-0.07 ± 0.37	7	10.0
$\Lambda \to \pi^- + p$ Indirect (Fig. 7b)	$\Lambda - \pi$	0.2	38.4 ± 3.0	3.3 ± 3.4	-0.5 ± 6.7	-0.01 ± 0.17	7	8.2
$\Sigma^0 \to \gamma + \Lambda$ (Fig. 8)	$\Sigma^0 - \gamma$	2 Mev	34.5 ± 2.7	0.6 ± 3.0	0.3 ± 6.1	0.01 ± 0.18	8	2.9

C. Production Ratios for K^- Interactions at Rest

The number of Σ^+ and Σ^- hyperons produced at rest is readily available from Table VI. The number of Σ^0 and Λ hyperons can be calculated using Table VI and the $\Lambda/(\Sigma^0+\Lambda)$ ratio of 0.186 ± 0.017. The numbers obtained in this way yield the ratio $\Sigma^-: \Sigma^+: \Sigma^0: \Lambda = 1553: 722: 977: 223$. The reaction amplitudes can then be calculated and resolved into I-spin-0 and I-spin-1 channels for Σ production. The results can be expressed in terms of the ratio of I-spin-0 and I-spin-1 amplitudes for the Σ mode and their relative phase, plus the ratio of the Λ I-spin-1 amplitude to the Σ I-spin-1 amplitude (see Appendix C). These quantities (after phase-space corrections) have been determined to be:

$$\left| \frac{A_{\Sigma_1}}{A_{\Sigma_0}} \right| = 0.37 \pm 0.06,$$

$$\cos \phi_{\Sigma_0 \Sigma_1} = 0.70^{+0.14}_{-0.10},$$

and

$$\left| \frac{A_{\Sigma_1}}{A_{\Lambda_1}} \right| = 1.57 \pm 0.23 .$$

The scattering-length analysis (see Appendix C) predicts at-rest properties for the K^--p system, and these predictions have been entered in the first row of Tables XIV and XVI for the two solutions found by a fit to all the data of this experiment.

D. Hyperon Production by In-Flight K^-p Interactions

Interactions of the K^--p system at low energies provide a contrast to the more conventional low-energy interactions of pions and nucleons. In the case of the K^--p system, there are several absorption channels available, and interactions through these channels are so strong that they dominate the behavior of the interactions even in the elastic channels. Both of the scattering-length solutions that have been found to fit the data of this experiment reveal the same general property of having almost pure imaginary scattering lengths as a result of the strong absorption. In fact, the most striking difference between the two solutions is the behavior of the phase between the I-spin-0 and I-spin-1 absorption amplitudes, and its influence on the Σ^-/Σ^+ ratio (see Tables XIV and XVI). The better of the two solutions tends to predict $\Sigma^-/\Sigma^+ \approx 1$ and slowly varying, while the other solution predicts $\Sigma^-/\Sigma^+ \approx 1$ and rapidly falling.

No attempt has been made to correct for p-wave effects because the magnitude of the p-wave contribution is not known. The angular distributions for K^--p interactions are quite consistent with isotropy, and the s-wave theory seems to fit quite well; therefore, the data of this experiment are probably not sufficiently definitive to justify a fit with more parameters using a non-zero effective-range theory. Further data soon will be available from a recent K^--p experiment now in the process of being analyzed.

E. Current Extensions of the Analysis

Several variations of the scattering length analysis are being currently used to refit the data. The separate Σ^- and Σ^+ are being combined into a single $(\Sigma^- + \Sigma^+)$ cross section in order to minimize the effects of phase shifts from the pion-hyperon channels as a function of energy. $(\Sigma^+ + \Sigma^-)$ is independent of the phase ϕ between the I-spin-0 and I-spin-1 Σ channels. Also, a fit to the data will be attempted without using the higher energy interactions. An attempt will be made to subtract out p-wave interactions in order to investigate the dependence of the parameters on the p-wave contamination. The six-dimensional χ^2 space will be investigated from starting points other than the Dalitz starting values used in this report.

A similar scattering length analysis of a recent K^--p experiment (in the same bubble chamber) is under way. The separated beam used in the new experiment is much richer in K^-'s, and has a much smaller number of background tracks. Experience with the bubble chamber has also led to improvements in the quality of the bubble chamber photographs. The number of events available for anlaysis will be about three times the number reported in this experiment.

ACKNOWLEDGMENTS

This experiment would not be possible without the generous contributions of time and effort on the part of many people. I am particularly indebted to Dr. Luis Alvarez, Dr. Joseph Murray, Dr. Arthur Rosenfeld, Dr. Ronald Ross and Dr. Frank Solmitz. I wish also to express my appreciation to Mrs. Karen Profet and Mr. Jim Neufeld for their aid during the processing of the events in this experiment. The cooperation of the Bevatron staff and bubble chamber operating crew, headed by Messrs. Robert Watt and Glen Eckman, was most helpful during the bubble chamber run.

APPENDICES

A. DATA-PROCESSING PROGRAMS

Analysis of the 15-inch bubble chamber film was accomplished with the aid of a series of 704 programs, principally PANG, KICK, EXAMIN, MERGE, and PATH.

1. PANG

Program PANG is designed to analyze tracks in the 15-inch hydrogen bubble chamber.[18] The analysis includes spatial reconstruction of points measured along the track (from the most suitable two of the four views for the track under consideration), and a least-squares fitting of these points with a space curve. The program reconstructs points in space, taking into account such optical properties of the chamber as the index of refraction of the liquid hydrogen, deflections of several glass windows, the effect of several mirrors, and lens distortion. The curve, which is fitted to the reconstructed track points, includes terms that modify its shape to account for variations of the magnetic field along the track, and change of curvature resulting from energy loss of the particle. Momentum, position, and angles at each end of each track are calculated. Also, errors for most of these quantities are computed, including the effect of Coulomb scattering.

The input information is originally in the form of IBM cards. The input cards include "master cards" containing film measurements of fiducials in the chamber and certain other information pertaining to the event being considered. The rest of the cards are "track cards," each containing film positions of points along a track as measured on a digitized projection microscope.

The output is of three types. One type is the "on-line printout," in which error indications are printed out via the on-line IBM printer each time a defect is detected in the input information. There is also an off-line printout; after the results of the calculations of an event are written on a tape, the tape is "printed" on a high-speed printer.

The third output is a tape containing information corresponding to that on the off-line printer tape, but in binary form more suitable for use by subsequent programs.

The running time per track is one or two seconds, and the time for a typical event in this experiment is about six seconds.

2. KICK

The KICK program is designed to extract, from the track information of PANG, the best values of the parameters describing an interaction or decay vertex.[19] If it is possible to measure the direction and momentum of all the particles at a vertex, then the kinematics of the vertex are overdetermined. The measured values of angles and momentum for each track must be adjusted to be consistent with the four constraints of energy-momentum conservation. If the direction or momentum of a particle cannot be measured (for example, a momentum measurement may not be available for a short track), one or more of the constraints may be used to calculate the missing quantities, and the measured values are then adjusted to satisfy the constraints still remaining. The KICK program handles five constraint classes corresponding to the number of missing variables at the vertex (the fifth class is merely a calculation using the four equations of constraint to calculate four missing variables).

A least-squares criterion was used to adjust the measurement values. The PANG program generally computes three variables for each track: the momentum, and two angles in terms of spherical coordinates. The errors in these quantities are also computed by PANG. The adjusted variables are found by minimizing the following equation:

$$\chi^2 = \sum_{\substack{i=1 \\ j=1}}^{N} (x_i - x_i^m) G_{ij} (x_j - x_j^m),$$

subject to the equations of constraint, $F_\lambda(x_i) = 0$, and $\lambda = 1, C$,

where x_i = adjusted variable,

x_i^m = measured variable,

$G_{ij}^{-1} = \overline{\delta x_i^m \, \delta x_j^m}$ = error matrix,

N = number of measured variables,

$F_\lambda(x_i)$ = energy-momentum conservation, and

C = 4-(number of missing variables).

The chi-square function should be distributed as a χ^2 distribution with the number of degrees of freedom equal to C. In actuality, the χ^2 distribution for the events analyzed in this experiment deviates somewhat from the expected distribution. A study of this problem seems to indicate that the errors computed in PANG are about 15% too small, and that the error distributions of the variables measured by PANG have a small non-gaussian tail, which probably reflects the effects of small-angle single scatters and turbulence of the liquid hydrogen in the chamber. There is also weak evidence from the data that the momentum estimates from curvature may be too small by about 3%; however, this does not have any significant effect on the answers, and a correction has not been included in the analysis (well-determined events seem to depend principally on the angular measurements). More detailed discussion of the χ^2 distribution is available in Ref. 1.

The KICK program computes as output the adjusted values for momentum and angles at the vertex considered (as well as a complete error matrix), the value of χ^2, and certain information about the direction and magnitude of the adjustments to the PANG measured values (for studies of systematic errors in the PANG estimates). The input to KICK is the binary tape produced by PANG, and the output is another binary tape. The running time is about the same as PANG, i.e., about 6 seconds per event.

3. EXAMIN

The EXAMIN program processes the binary tape from KICK. The KICK output for an event is examined to see if the event has been fitted successfully (i.e., has an acceptable χ^2), and successful fits are used to compute the final physical parameters describing the event. There are usually about 50 such parameters per event, and these are written on a binary tape to be merged into a library of events. Unsuccessful fits are rejected and information that might be useful for reprocessing the event is printed out. Pathlength for the interactions is also computed at this point.

4. MERGE

The MERGE program accumulates the results of the accepted fits in such a way that an up-to-date sample of events is always available on a binary tape for summary calculations based on the whole experiment. The program also keeps track of the location of results for events at each stage of computation; it records which events have been rejected and why, and in general handles the bookkeeping chores.

5. PATH

PATH is a special program that processes the PANG output for the K^- tracks that went through the chamber, and calculates the length of K track in the fiducial volume and the K^- momentum at an entrance plane in the chamber. This pathlength information, together with the pathlength information for the events (calculated in EXAMIN) determines the pathlength used to establish the cross sections.

B. Maximum-Likelihood Estimate of the Number of Interactions per Momentum Interval

In the analysis of this experiment it was always necessary to consider two types of interactions; those arising from the discrete set of stopped K mesons and those created by K-p interactions over a continuum of K momenta. Any individual event cannot be classified unambiguously as one or the other; however, all the events in the experiment taken together can be used to estimate the distribution of events in the two classes. To this end, the number of events in each of several momentum intervals was estimated according to the maximum-likelihood method.[20]

An attempt was made to fit all the hyperon productions as in-flight interactions; however, the kinematics program frequently only gave a fit with zero K momentum. Hence, the measurements of the events also can be divided into two classes corresponding to at-rest fits and in-flight fits. The contributions to the likelihood calculations were different for each class.

1. Formulation of the Likelihood Problem

The likelihood function is defined as the probability of observing an experimental measurement as a function of the set of parameters α_i to be estimated. The set of parameters that provides the highest probability of observing the experimental results is taken as the best estimate of the parameters. In this particular case, the problem is one of determining the best estimates for the true number of events expected in several momentum intervals. This task is confounded in two ways: first, there is the usual problem of statistical fluctuation; that is, even if one knows the number of events expected, there is a statistical uncertainty in the number observed. Secondly, the momentum of a particle can not be measured with infinite precision, and therefore, an event taking place at one momentum will have another observed momentum, and will possibly be included in another momentum interval.

More specifically, the probability of observing a certain number of events in a set of momentum intervals is really a compound probability having two important factors. First there is the probability that there will be an event in the true momentum interval p, p + dp. Secondly, there is the probability that, given such an event, the event should be measured ("observed") in the momentum interval p_o, $p_o + dp_o$. This combined probability can be written as

$$d^2P = \left[P_t(p)\,dp\right]\left[P_o(p, p_o)dp_o\right],$$

where P_t = a theoretical expression for the probability of an event at true momentum p, a function of one or more parameters a_i, and

P_o = the probability that p should be observed as p_o. One can then sum over all true p to give the total probability of observing any event in the interval p_o, $p_o + p_o$ as

$$dP = \left[\int P_t(p)\, P_o(p, p_o)dp\right] dp_o .$$

In the particular case being considered, there is (in addition to the continuum of probabilities represented by P_t) a discrete probability representing the probability of an event occurring at rest.

For interactions that give in-flight fits, the differential probability dP for observing an interaction at observed K-momentum p_o is then given by:

$$\frac{dP(a_i)}{dp_o} = \frac{1}{N_T}\left\{\int_0^\infty \frac{dn(a_i)}{dp}\, C(p)\, P_o(p, \Delta p, p_o)dp + N_R\, C(0) P_o(0, \Delta p, p_o)\right\} .$$

In the case of the at-rest fits, the probability of seeing an interaction is given by

$$P(a_i) = \frac{1}{N_T} \left\{ \int_0^\infty \frac{dn(a_i)}{dp} C(p) \left[1 - \int_{p_{min}}^\infty P_o(p, \Delta p, p_o) dp_o \right] dp \right.$$

$$\left. + N_R \, C(0) \left[1 - \int_{p_{min}}^\infty P_o(p, \Delta p, p_o) dp_o \right] \right\} ,$$

where $\frac{dn(a_i)}{dp}$ = number of events per momentum interval as a function of the parameters a_i, $\left[\frac{dn(a_i)}{dp} \propto \sigma(a_i, p) \frac{d\ell}{dp} \right]$,

$C(p)$ = probability of passing acceptance criteria on hyperon length and orientation, assuming a true momentum p,

$P_o(p, \Delta p, p_o)$ = probability that an event at true momentum p should be observed between momentum p_o and $p_o + dp_o$, given measurement error Δp,

p_{min} = measured momentum, below which an event is considered to fit an at-rest interaction, and

N_R = estimate of the true number of at-rest interactions.

The true total number of acceptable events is then

$$N_T = N_R \, C(0) + \int_0^\infty \frac{dn(a_i)}{dp} C(p) dp.$$

The probability expressed in this way is normalized to unity when one integrates over all observed K-momenta p_o for in-flight fits, and adds in the probability of observing an at-rest fit.

The log of the likelihood function is formed by summing the log of the probability for each event:

$$\ln L = \sum_{i=1}^{N_1} \ln P_i(a_i) + \sum_{j=1}^{N_2} \ln \frac{dP_j(a_i)}{dp_o}$$

where N_1 = number of at-rest fits, and

N_2 = number of in-flight fits.

The estimated values of the a_i are then taken as the values that maximize the function $\ln L$.

In practice, $\frac{dn(a_i)}{dp}$ was parameterized by assigning a parameter to each momentum interval considered, so that

$\frac{dn}{dp} = a_i$ in the ith interval.

For the Σ interactions, $P_o(p, \Delta p, p_o)$ was taken as

$$P_o(p, p_o, \Delta p) = \frac{1}{\sqrt{2\pi}\,\Delta p} \exp\left[-1/2 \left(\frac{p-p_o}{\Delta p}\right)^2\right]$$

where p_o, Δp are the observed momentum and its error estimate. The Σ acceptance-criterion C was

$$C(p) = \exp\left[-t_c/\tau\right](\cos\theta_f - \cos\theta_b)/2 \quad ,$$

where t_c = time of flight for first 0.1 cm,

θ_f = forward cutoff angle (20 deg) in the K-p c.m. system.

θ_b = backward cutoff angle (20 deg) in the K-p c.m. system.

The Λ analysis was more difficult because the K momentum error distribution is skew. The actually observed quantity is the curvature k_o of the K track at the center of the track; the momentum at the end of the track is found by computing the momentum p at the center of the track ($p \propto 1/k_o$), and determining the momentum loss to the end of the track. Therefore, k_o and Δk (the curvature and its error

estimate) were taken as the observed quantities, and the probability of observing an event was expressed in terms of them:

$$P_o(p, \Delta k, k_o) = \frac{1}{\sqrt{2\pi}\,\Delta k} \exp\left[-1/2\left(\frac{k(p) - k_o}{\Delta k}\right)^2\right]$$

where k(p) = curvature corresponding to a momentum p at the interaction end of the track,

and C(p) was taken as $\left(\exp\left[-t_c/\tau\right] - \exp\left[-t_m/\tau\right]\right)$,

where t_c = time of flight for first 0.1 cm,

t_m = time of flight to nearest interaction boundary, and

τ = lambda lifetime.

2. The Likelihood Solutions

The likelihood was formulated with N_T constrained to be the observed number of events, making $N_R C(0)$ a dependent variable defined by the equation for N_T. The likelihood was also formed with a Poisson distribution for the total number of accepted events, and with N_R taken as a parameter. The estimates for the central values of the parameters were the same with both methods; however, the variance matrix estimated for the parameters on the basis of the formula

$$(V_{ij})^{-1} = - \frac{d^2 \ln L}{d\alpha_i \, d\alpha_j} = (\overline{\delta\alpha_i \, \delta\alpha_j})^{-1}$$

was somewhat different. For N_T fixed, the character of the matrix V was that of a multinomial distribution with appreciable correlations between all parameters. The Poisson formulation gave the more acceptable errors, which were used in the further analysis to determine the scattering length parameters (Appendix C).

The raw data, the maximum-likelihood estimates, and the variance matrices for hyperon production as a function momentum, are displayed in Tables VIII, IX and X. The corrections to the raw data, and the correlation terms between the at-rest group and the low-momentum intervals, indicate the extent of the correction for the at-rest vs in-flight ambiguity. These correlation terms also indicate the momentum resolution for in-flight events of this experiment; in particular, the off-diagonal elements do not become small for the Σ events unless the momentum intervals are lumped into 50 Mev/c intervals. If intervals are combined into larger intervals, a new variance matrix is easily computed by merely adding together appropriate elements of the variance matrix V. As an example, consider the following case:

Table VIII

Summary of numbers of events as a function of K momentum for Σ^- production

K^- lab momentum interval (Mev/c)	Number events observed	Corrected number of events	Variance matrix for estimate of corrected number of events									
			0-50	50-75	75-100	100-125	125-150	150-175	175-200	200-225	225-250	250-275
0-50	1101	1103.0	1105.3									
50-75	7	8.7	-2.4	15.3								
75-100	14	11.2	0.0	-4.4	18.2							
100-125	12	8.5	-0.3	0.3	-2.5	17.1						
125-150	14	16.9	-0.1	0.0	-0.1	-6.7	27.6					
150-175	10	6.2	0.0	0.0	0.0	0.8	-4.2	14.4				
175-200	24	29.8	0.0	0.0	0.0	-0.1	0.4	-5.6	44.0			
200-225	16	15.8	0.0	0.0	0.0	0.0	-0.1	1.0	-10.6	32.3		
225-250	9	7.9	0.0	0.0	0.0	0.0	0.0	-0.2	2.0	-8.1	17.7	
250-275	5	3.7	0.0	0.0	0.0	0.0	0.0	0.0	-0.3	1.3	-3.5	6.2

The symmetric elements of the variance matrix $(\overline{\delta N_i\ \delta N_j})$ have not been duplicated.

Table IX

Summary of numbers of events as a function of K momentum for Σ^+ production

K^- lab momentum interval (Mev/c)	Number events observed	Corrected number of events	Variance matrix for estimate of corrected number of events								
			0-75	75-100	100-125	125-150	150-175	175-200	200-225	225-250	250-275
0-75	483	484.4	485.6			The symmetric elements of the variance matrix					
75-100	5	2.6	-10.2	6.6		$(\overline{\delta N_i\ \delta N_j})$ have not been duplicated.					
100-125	12	14.2	0.0	-3.5	26.0						
125-150	11	6.6	-0.1	0.8	-9.6	24.3					
150-175	18	21.0	-0.1	-0.2	1.7	-9.7	35.1				
175-200	12	14.7	0.0	0.0	-0.4	1.1	-7.0	28.2			
200-225	18	17.0	0.0	0.0	0.1	-0.2	1.4	-8.0	29.3		
225-250	15	15.3	0.0	0.0	0.0	0.0	-0.2	0.9	-6.1	24.1	
250-275	4	3.2	0.0	0.0	0.0	0.0	0.0	0.1	0.6	-3.4	6.1
275-300	1	-	-	-	-	-	-	-	-	-	-

Table X

Summary of numbers of events as a function of K momentum for $\Sigma^0 + \Lambda$ production

K^- Lab Momentum Interval (Mev/c)	Number Events observed	Corrected number of events	Variance matrix for estimate of corrected number of events					
			0-125	125-150	150-175	175-200	200-225	225-250
0-125	654	680.2	1108.7		The symmetric elements of the variance matrix $(\overline{\delta N_i \, \delta N_j})$ have not been duplicated.			
125-150	67	42.8	-943.3	2511.0				
150-175	34	38.8	743.0	-2263.4	2430.2			
175-200	22	6.9	-312.2	1023.3	-1247.8	866.7		
200-225	10	26.8	107.3	-371.1	498.4	-440.0	332.7	
225-250	11	2.9	-26.6	93.3	-128.7	120.6	-102.1	469.1

$$n_1, n_2, n_3, \ldots \begin{pmatrix} \overline{\delta n_1\, \delta n_1} & \overline{\delta n_1\, \delta n_2} & \overline{\delta n_1\, \delta n_3} \ldots \\ \overline{\delta n_2\, \delta n_1} & \overline{\delta n_2\, \delta n_2} & \overline{\delta n_2\, \delta n_3} \ldots \\ \overline{\delta n_3\, \delta n_1} & \overline{\delta n_3\, \delta n_2} & \overline{\delta n_3\, \delta n_3} \ldots \\ \vdots & \vdots & \vdots \end{pmatrix}$$

If we define $N = n_1 + n_2$, then clearly

$$\overline{\delta N\, \delta N} = \overline{\delta n_1\, \delta n_1} + \overline{\delta n_1\, \delta n_2} + \overline{\delta n_2\, \delta n_1} + \overline{\delta n_2\, \delta n_2}$$

and

$$\overline{\delta N \delta n_3} = \overline{\delta n_1\, \delta n_3} + \overline{\delta n_2\, \delta n_3}$$

and in general

$$\overline{\delta N\, \delta n_j} = \overline{\delta n_1\, \delta n_j} + \overline{\delta n_2\, \delta n_j}$$

This merging process can be repeated with the new set of variables, $(N, n_3, n_4, \ldots)$ and so forth, until the desired set of intervals is obtained. The same procedure may be used to estimate the error associated with the average of a cross section over several momentum intervals.

C. Determination of K^- – Nucleon Scattering Amplitudes

1. Parametrization of Low-Energy K^--p Interactions

Making the assumption of charge independence, it is possible to describe the K^--p system and its interactions in terms of isotopic spin-0 and spin-1 components. The interaction amplitudes for these two isotopic spin channels may then be expressed in terms of an s-wave phase-shift analysis to give

$$\sigma_{el} = (\pi/k^2) \left| \frac{\exp[2i\delta_0] - 1}{2i} + \frac{\exp[2i\delta_1] - 1}{2i} \right|^2$$

$$= (\pi/4k^2) \left| \frac{\exp[2i\delta_0] + \exp[2i\delta_1] - 2}{i} \right|^2 ,$$

$$\sigma_{ce} = (\pi/k^2) \left| \frac{\exp[2i\delta_0] - 1}{2i} - \frac{\exp[2i\delta_1] - 1}{2i} \right|^2$$

$$= (\pi/4k^2) \left| \frac{\exp[2i\delta_0] - \exp[2i\delta_1]}{i} \right|^2 ,$$

$$\sigma_0 = (\pi/k^2)\,(1 - |\exp 2i\delta_0|^2) ,$$

and

$$\sigma_1 = (\pi/k^2)(1 - |\exp 2i\delta_1|^2),$$

where σ_{el} = elastic scattering cross section ,

σ_{ce} = charge exchange cross section ,

σ_0 = absorption in I-spin 0 channel,

and

σ_1 = absorption in I-spin 1 channel ,

k = wavenumber in c.m. system. (i.e., $k=(p/197.2)\text{fermi}^{-1}$, where p is momentum in Mev/c) ,

δ_0 = complex phase shift for the I-spin-0 channel ,

and

δ_1 = complex phase shift for the I-spin-1 channel.

An effective range expansion gives

$$k \cot \delta_0 = 1/A_0 + 1/2\, R_0 k^2 + \ldots$$

$$k \cot \delta_1 = 1/A_1 + 1/2\, R_1 k^2 + \ldots$$

The effective range has been taken as zero ($R_0 = R_1 = 0$), leaving only two complex scattering lengths A_0 and A_1 to represent the K^--p system at low energies. In terms of these scattering lengths the cross sections are

$$\sigma_{el} = \pi \left| \frac{A_0 + A_1 - 2ikA_0A_1}{(1-ikA_0)(1-ikA_1)} \right|^2 ,$$

$$\sigma_{ce} = \pi \left| \frac{A_0 - A_1}{(1-ikA_0)(1-ikA_1)} \right|^2 ,$$

$$\sigma_0 = \frac{2\pi}{k} \operatorname{Im} A_0 \left| \frac{1}{1-ikA_0} \right|^2 ,$$

and

$$\sigma_1 = \frac{2\pi}{k} \operatorname{Im} A_1 \left| \frac{1}{1-ikA_1} \right|^2 .$$

Since there are four independent parameters (the components of A_0 and A_1) and four observable cross sections, it would seem that a measurement of the cross sections at a single energy should provide enough information to determine A_0 and A_1. Unfortunately, this is not the case. There exist four sets of phase shifts capable of producing a given set of cross sections at one energy. To see this, consider the following representation of the phase shifts:[21]

Let $\vec{V}_0 = \dfrac{\exp[2i\,\delta_0]}{i}$ in the complex plane, and $\vec{V}_1 = \dfrac{\exp[2i\,\delta_1]}{i}$ in the complex plane.

Then, if one knows σ_0 and σ_1,

$$\left|\vec{V}_0\right| = \sqrt{1-\frac{\sigma_0 k^2}{\pi}} ,$$

and

$$\left|\vec{V}_1\right| = \sqrt{1-\frac{\sigma_1 k^2}{\pi}} ;$$

and from σ_{el} and σ_{ce},

$$\left|\vec{V}_0 + \vec{V}_1 + 2\hat{n}\right| = \sqrt{\frac{4k^2\sigma_{el}}{\pi}} ,$$

and

$$\left|\vec{V}_0 - \vec{V}_1\right| = \sqrt{\frac{4k^2\sigma_{ce}}{\pi}} ,$$

where $\hat{n}$ is a unit vector along the imaginary axis.

These four conditions are illustrated diagramatically in Fig. 19, and it is apparent that a reflection through the real axis or a reflection through the vector $\vec{V}_0 + \vec{V}_1$ produces new and equally suitable solutions. These four solutions are designated a^+, b^+, a^- and b^- as indicated in the figure. The + and - refer to symmetry about the real axis, and the a and b refer to symmetry about $\vec{V}_0 + \vec{V}_1$.

The large mass difference between the $\bar{K}^0$-n and K^--p system (5.2 Mev), and the Coulomb interaction, make it necessary to break the strict assumption of charge independence. The zero-effective-range formalism has been extended to include these effects.[2, 22] The four-fold ambiguity in the scattering lengths persists in the modified theory. The mass difference and, most of all, the Coulomb effects, give rise to the following more complicated expressions for the cross sections:

$$\frac{d\sigma_{el}}{d\Omega} = \left| \frac{(\csc^2\theta/2)\exp\left[(2i/kB)\ln\sin\theta/2\right]}{2Bk^2} + \frac{C^2(x-ik_0(x^2-y^2))}{D} \right|^2 ,$$

$$\frac{d\sigma_{ce}}{d\Omega} = \frac{C^2 k_0}{k}\left|\frac{y}{D}\right|^2 ,$$

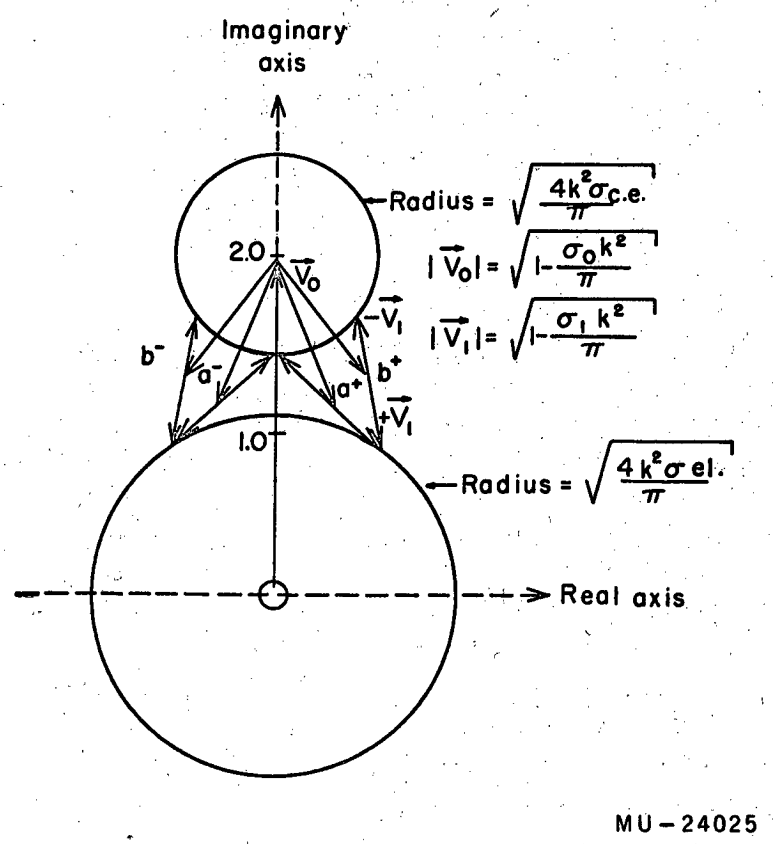

Fig. 19. The source of the 4-fold ambiguity in the scattering length theory is indicated diagramatically. The conventional identification (a^+, b^+, a^-, b^-) of each solution is indicated.

$$\sigma_0 = \frac{4\pi C^2 I_m A_0}{k} \left| \frac{(1-ik_0 A_1)}{D} \right|^2 ,$$

and

$$\sigma_1 = \frac{4\pi C^2 I_m A_1}{k} \left| \frac{(1-ik_0 A_0)}{D} \right|^2 .$$

Also, we have $D=(1-ixk_0)(1-ixC^2k(1-i\lambda))+C^2k_0k(1-i\lambda)y^2$

where $\theta = K^- - K^-$ scattering angle in the center-of-mass system,

$B = \hbar^2/\mu e^2$, the Bohr radius of the K^--p system,

$C^2 = (2\pi/kB)/(1-\exp[-2\pi/kB])$, the Coulomb penetration factor,

k_0 = wave number in $\overline{K}^0$-n system, taken positive imaginary below threshold,

$x = 1/2(A_1 + A_0)$,

$y = 1/2(A_1 - A_0)$,

$$\lambda \approx -(2/C^2kB)\left[\ln(2R/B)+g-\int_0^1 \frac{\sin^2 kRv}{v}\, dv\right],$$

$R \approx 1f$, range of nuclear interaction,

$g = \mathrm{Re}\,\psi(i/kB) + \ln(kB) + 2(0.5772)$,

and

$\psi = (d/dZ)\ln\Gamma(Z)$.

The functions $\int_0^1 \left[(\sin^2 kRv)/v\right] dv$, and $\mathrm{Re}\psi$ were evaluated by series expansions as follows:

$$\int_0^1 \frac{\sin^2 kRv}{v}\, dv = 1/2 \sum_{n=1}^{m} \frac{(2kR)^{2n}(-1)^{n+1}}{2n(2n!)} .$$

and

$$\mathrm{Re}\psi = \begin{cases} \ln(1/kB) + \dfrac{(kB)^2}{12} + \dfrac{(kB)^4}{120} + \dfrac{(kB)^6}{252}, & \text{with } kB < 1/5, \\[2ex] \dfrac{1}{(kB)^2}\left[\displaystyle\sum_{n=1}^{100} \dfrac{1/n}{n^2 + (1/kB)^2} + 0.501\times 10^{-4}\right] - 0.5772, & \text{with } kB > 1/5. \end{cases}$$

These functions are plotted in Figs. 20 and 21. The function λ is plotted for 2 values of R (0.5 and 1.0 fermi) in Fig. 22.

Now consider the final states of the two I-spin absorption channels:

$$\sigma_0 = 3\sigma(\Sigma^0\pi^0),$$

and

$$\sigma_1 = [\sigma(\Sigma^+\pi^-) + \sigma(\Sigma^-\pi^+) - 2\,\sigma(\Sigma^0\pi^0)] + \sigma(\Lambda\pi^0)$$

Let the I-spin-1 and I-spin-0 matrix elements for the Σ channels be M_1 and M_0. Let the I-spin-1 matrix elements for the Λ channel be N_1. Let these elements be normalized so that

$$\sigma(\Sigma^+\pi^-) = \left|M_0/\sqrt{3} - M_1/\sqrt{2}\right|^2,$$

$$\sigma(\Sigma^-\pi^+) = \left|M_0/\sqrt{3} + M_1/\sqrt{2}\right|^2,$$

$$\sigma(\Sigma^0\pi^0) = \left|-M_0/\sqrt{3}\right|^2,$$

$$\sigma(\Lambda\pi^0) = \left|N_1\right|^2,$$

and

$$\sigma_0 = \left|M_0\right|^2, \quad \sigma_1 = \left|M_1\right|^2 + \left|N_1\right|^2.$$

At this point, two new parameters are introduced. Although σ_0 and σ_1 are already determined by A_0 and A_1, it is still necessary to specify the phase between M_0 and M_1 as well as the relative magnitude of M_1 and N_1. These parameters are defined in terms of the following

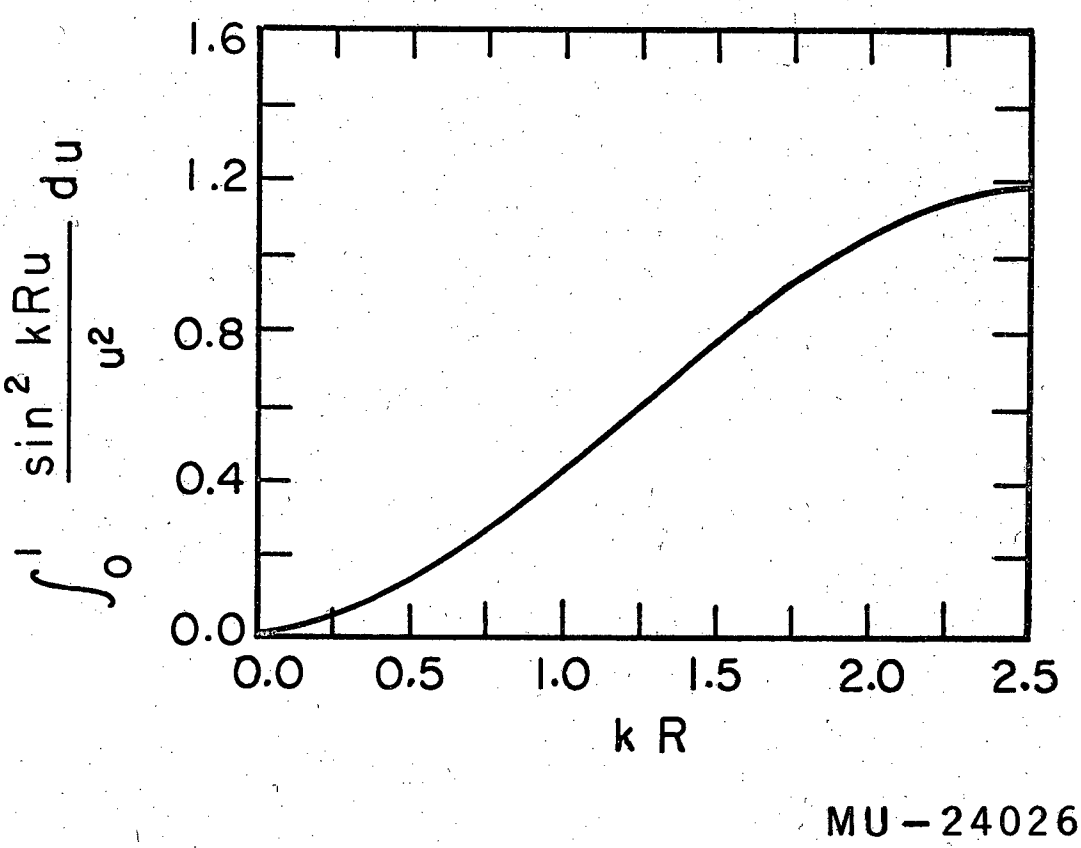

Fig. 20. The function $\int_0^1 \frac{\sin^2 kRu}{u^2} du$ plotted as a function of kR.

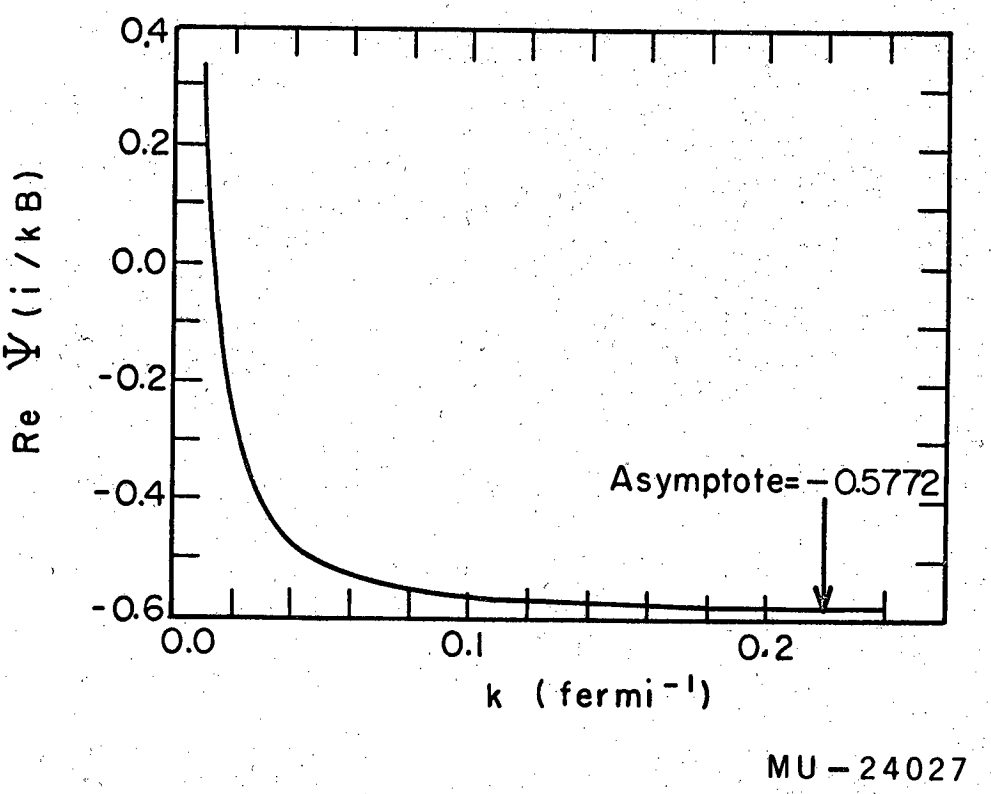

Fig. 21. The function Re ψ(i/kB) plotted as a function of k. (B = 83.6 f.)

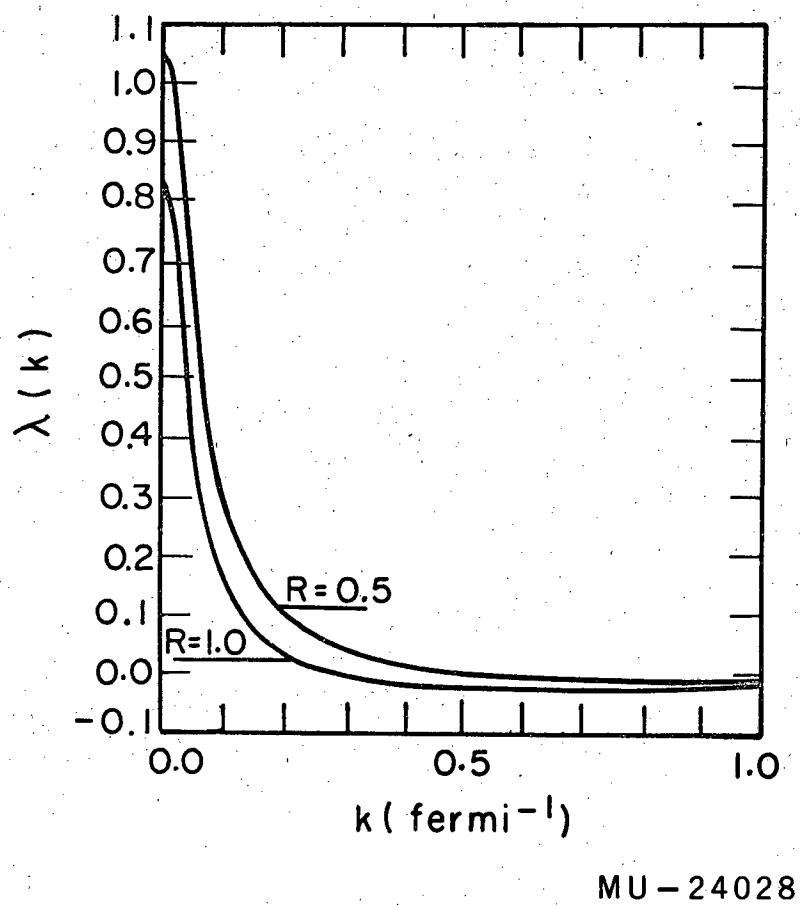

Fig. 22. Coulomb corrections are largely represented by the behavior of the function λ. Here λ is plotted as a function of k for R = 1.0 f. and R = 0.5 f.

equations:

$$\epsilon = \sigma(\Lambda\pi^0)/\sigma_1 = |N_1|^2/(|M_1|^2 + |N_1|^2),$$

and

$$\frac{\sigma(\Sigma^-\pi^+)}{\sigma(\Sigma^+\pi^-)} = \frac{|M_0|^2/3 + \sqrt{2/3}\,|M_0|\,|M_1|\cos\phi + |M_1|^2/2}{|M_0|^2/3 - \sqrt{2/3}\,|M_0|\,|M_1|\cos\phi + |M_1|^2/2},$$

where now

$$|M_0|^2 = \sigma_0 ,$$

$$|M_1|^2 = \sigma_1(1-\epsilon) ,$$

and

$$|N_1|^2 = \sigma_1(\epsilon) .$$

The assumption is made that the final state interactions ($\Sigma\pi$ and $\Lambda\pi$) do not vary rapidly with energy, and that the small variation in phase space with changing K^--p energy may be neglected. With these assumptions, it can be shown that ϵ becomes a constant[2] and the energy dependence of ϕ is governed by the known behavior of the I-spin-0 and I-spin-1 amplitudes according to the relation

$$\phi = \phi(E_T) + \arg\,[(1-ik_0A_1)/(1-ik_0A_0)] ,$$

where $\phi(E_T)$ is the phase for K^--p interactions at the $\bar{K}^0$-n threshold. There is another ambiguity introduced by the uncertainty of the sign of ϕ at a single energy, i.e., $\cos\phi = \cos -\phi$. $\phi(E_T)$ may be derived from the ratio $\gamma = \Sigma^-/\Sigma^+$ for sigmas produced by K interactions at rest. The γ is a more convenient parameter than $\phi(E_T)$, in the sense that it is a well-known experimental number and is less coupled to the other parameters during the fitting procedure.

The six parameters represented by A_0, A_1, ϵ and γ constitute a description of the K^--p interactions of this experiment, subject to the assumptions made above. More detailed investigation of these assumptions have been made by Dalitz and Tuan,[2] as well as Jackson, Ravenhall, and Wyld,[22] using the K-matrix reaction theory.

2. Fitting the Data

The theoretical description of the K^--p system at low energies must be in agreement with two types of experimental data. About 90% of the hyperons are produced by K^- mesons which interact at rest. These events provide statistically well determined production ratios between all the hyperon channels at zero energy in the K^--p system. The remaining 10% of the hyperons are produced by K^- mesons interacting in flight, and it is these events, taken with the K^--p elastic and charge-exchange scattering, which establish the energy dependence of the K^--p interactions.

The phenomenological theory presented in the previous section was fitted to 64 pieces of experimental data. In order to estimate the values of the six parameters which best describe the observed data, a χ^2 estimator was formed, with a contribution to the χ^2 from each of the 64 measurements listed in Table XI. The values of the parameters giving a minimum in the χ^2 were taken as the best estimates for the parameters.

More specifically, the χ^2 was of the form

$$\chi^2 = \sum_{i=1}^{7} \left(\frac{x_c^{\,i} - x_o^{\,i}}{\Delta x_o^{\,i}} \right)^2 + \sum_{j=1}^{8} \tilde{y}^{\,j} \cdot (G^j)^{-1} \cdot y^j ,$$

where $x_c^{\,i}$ = calculated value of observable data,

$x_o^{\,i}$ = experimental value of observable data,

$\Delta x_o^{\,i}$ = error estimate,

y^j = a vector difference between calculated and observed values for a set of correlated observables,

and G^j = error matrix (variance matrix) for a set of correlated observables.

The solution was defined as that set of parameters such that

$$\frac{\partial \chi^2}{\partial \alpha_i} = 0, \text{ with } i = 1, 6$$

Table XI

Contributions to the χ^2 estimate

Nature of the data	Statistical handling	Momentum range (Mev/c)	No. of Terms	χ^2 Contribution, Solution I	χ^2 Contribution, Solution II
K^--p elastic scattering cross section as a function of 7 momenta in four cos θ_{K-K} intervals (-1.0, 0.85), (0.85, 0.90), (0.90, 0.95), (0.955, 0.966)	7 cross sections per cos θ_{K-K} interval with full variance matrix between momentum intervals	100-275	7	7.56	15.21
		100-275	7	2.66	3.73
		100-275	7	1.79	1.91
		100-275	7	3.93	3.49
K^--p charge-exchange cross section	7 cross sections with full variance matrix between momentum intervals	100-275	7	2.14	2.20
Σ^- production cross section	9 cross sections with full variance matrix between momentum intervals	50-275	9	9.32	11.80
Σ^+ production cross section	8 cross sections with full variance matrix between momentum intervals	75-275	8	10.76	7.20
$(\Sigma^0 + \Lambda)$ production cross section	5 cross sections with full variance matrix between momentum intervals	125-250	5	13.19	15.40
$\Lambda/(\Sigma^0 + \Lambda)$ branching ratio	4 ratios treated as independent quantities	150-250	4	6.28	9.28
At-rest hyperon production	3 ratios treated as independent quantities	at rest	3	0.29	3.29

where α_i are the six parameters of the theory.

The minimum in the χ^2 function was found by numerically evaluating the first and second derivatives of the function with respect to each variable, and then moving the one variable which predicted the greatest reduction in the chi square. In some cases, an alternate procedure was used to locate the minimum in the chi square, making use of a quadradic expansion of the form

$$\chi^2 = \sum_{i,j=1}^{6} (\alpha_i - \alpha_i^C) D_{ij} (\alpha_j - \alpha_j^C) + \sum_{k=1}^{6} (\alpha_k - \alpha_k^C) E_k + F ,$$

where α_i^C = value of parameters at point of expansion,

D_{ij} = matrix (symmetric) evaluated by computing χ^2 for sets of α_i in the nieghborhood of α_i^C,

E_k = Vector evaluated by computing χ^2 for sets of α_i in the neighborhood of α_i^C,

and

$F = \chi^2$ at α_i^C.

Then, differentiating, one obtains

$$\frac{\partial \chi^2}{\partial \alpha_\ell} = 2 D_{\ell j} (\alpha_j^* - \alpha_j^C) + E_\ell = 0,$$

or

$$(\alpha_j^* - \alpha_j^C) = -1/2 D_{j\ell}^{-1} E_\ell ,$$

where α_j^* is the new estimate of the parameters at the χ^2 minimum. This procedure was repeated several times until the parameters no longer moved significantly.

The starting values chosen for the parameters were the estimates recently calculated by Dalitz for the a^+, a^-, b^+ and b^- solutions.[23] The a^+ and b^- starting values led to the same minimum, and the a^- and b^+ starting values led to a second lower minimum. Both of the possible phases for ϕ were followed for each of the four starting points. Quite

small steps were taken in seeking the minimum, in order that other minima would not be skipped over. The starting values and the solutions derived from them are presented in Table XII.

The values of the parameters giving the lowest χ^2, the matrix D, and the variance matrix for these parameters, are given in Tables XIII and XV. The matrix D allows predictions of the change in χ^2 which are good to about 30% for variations of parameters within a range of 1 or 2 standard deviations of the values at the minimum. The χ^2 space appears to be skew for several of the parameters.

Table XII

Scattering length parameters that best fit the data, and their starting values (See Appendix C)

	Solution	a_0(f.)	b_0(f.)	a_1(f.)	b_1(f.)	γ	ϵ	χ^2	Probability of exceeding χ^2
Starting Values	a^-	-0.75	2.00	-0.85	0.21	2.15	0.41	92.44	0.003
	b^+	1.15	2.00	0.70	0.25	2.15	0.41	103.33	0.0002
Final Values	I	-0.220	2.742	0.019	0.384	2.153	0.403	57.914	0.48
Starting Values	a^+	0.05	1.10	1.45	0.35	2.15	0.41	120.78	<0.00001
	b^-	-1.85	1.10	-0.10	0.65	2.15	0.41	128.10	<0.00001
Final Values	II	-0.592	0.964	1.202	0.562	2.040	0.391	73.494	0.083

Table XIII

Properties of the χ^2 space in the vicinity of solution I

Parameters	a_0(f.)	b_0(f.)	a_1(f.)	b_1(f.)	γ	ϵ
Central values	-0.220	2.742	0.019	0.384	2.153	0.403
Uncertainties of central values	1.07	0.31	0.33	0.075	0.16	0.027
Variance matrix V ($V = \overline{\delta\alpha_i \, \delta\alpha_j}$)						
a_0	1.15		Symmetric elements of the matrix V have not been duplicated.			
b_0	0.12	0.099				
a_1	0.28	0.033	0.11			
b_1	-0.051	-0.0092	-0.0090	0.0056		
γ	-0.052	0.0074	-0.011	-0.00065	0.027	
ϵ	-0.0098	0.00032	-0.0012	-0.00016	-0.00028	0.00072
Expansion matrix D ($\chi^2 \cong \sum_{i,j} \Delta\alpha_i \, D_{ij} \, \Delta\alpha_j + 57.91$)						
a_0	12.13		Symmetric elements of the matrix D have not been duplicated.			
b_0	-0.10	25.91				
a_1	-24.25	-6.24	73.67			
b_1	74.82	29.92	-116.52	926.21		
γ	-4.45	-9.26	22.62	-9.13	85.85	
ϵ	136.58	-20.80	-214.51	991.50	14.65	4471.0

Table XIV

Properties of the scattering-length solution I

(A_0=-0.220+i2.742, A_1=0.019+i0.384, γ=2.153, ϵ=0.403, χ^2=57.9)

K^- lab momentum (Mev/c)	Cross sections (mb)							Production ratios			Phase
	σ_{el}	σ_{ce}	σ_0	σ_1	σ_{Σ^-}	σ_{Σ^+}	$\sigma_{\Sigma^0+\Lambda}$	$\Lambda/(\Sigma^0+\Lambda)$	Σ^-/Σ^+	$\frac{(\Sigma^-+\Sigma^+)}{(\Sigma^0+\Lambda)}$	$\phi_{\Sigma_0-\Sigma_1}$
at-rest	-	-	-	-	-	-	-	0.21	2.15	1.89	60.3
37.5	1374.3	0.0	2178.9	425.4	567.4	286.0	448.8	0.19	1.98	1.90	62.4
62.5	356.2	0.0	1000.5	171.5	242.9	141.9	201.3	0.17	1.71	1.91	67.3
87.5	201.3	0.0	594.5	83.1	122.6	100.4	115.8	0.14	1.22	1.93	80.9
112.5	122.6	27.1	278.5	86.4	55.8	62.8	63.8	0.27	0.89	1.86	94.1
137.5	92.6	23.6	172.9	71.1	37.3	41.5	43.1	0.33	0.90	1.83	93.4
162.5	74.7	19.4	117.2	58.8	26.9	29.7	31.4	0.38	0.91	1.81	93.0
187.5	62.5	15.8	84.0	49.4	20.4	22.4	23.9	0.42	0.91	1.79	92.7
212.5	53.6	13.0	62.7	42.1	16.0	17.5	18.9	0.45	0.92	1.77	92.5
237.5	46.8	10.8	48.4	36.4	13.0	14.0	15.4	0.48	0.92	1.75	92.3
262.5	41.4	9.1	38.3	31.7	10.7	11.5	12.8	0.50	0.93	1.74	92.1
287.5	37.1	7.7	30.9	28.0	9.0	9.7	10.8	0.52	0.93	1.73	92.0

Table XV

Properties of the χ^2 space in the vicinity of solution II						
Parameters	a_0(f.)	b_0(f.)	a_1(f.)	b_1(f.)	γ	ϵ
Central values	-0.592	0.964	1.202	0.562	2.04	0.391
Uncertainties of central values	0.46	0.17	0.060	0.15	0.18	0.023
Variance matrix V ($V = \overline{\delta a_i \, \delta a_j}$)						
a_0	0.21	Symmetric elements of the matrix V have not been duplicated.				
b_0	0.12	0.028				
a_1	-0.11	-0.0053	0.0036			
b_1	-0.051	-0.038	0.037	0.022		
γ	-0.043	-0.0028	-0.0041	0.012	0.033	
ϵ	-0.00049	-0.00032	0.00073	-0.00092	0.00061	0.00054
Expansion matrix D ($\chi^2 \simeq \sum_{i\,j} \Delta a_i \, D_{ij} \, \Delta a_j + 73.49$)						
a_0	41.55	Symmetric elements of the matrix D have not been duplicated.				
b_0	-40.74	139.44				
a_1	-42.25	129.38	102.14			
b_1	111.93	-100.92	-55.79	299.93		
γ	0.58	16.61	-7.93	11.59	57.50	
ϵ	258.58	-317.43	-184.09	609.90	-24.32	5022.5

Table XVI

Properties of the scattering-length solution II

(A_0=-0.592+i0.964, A_1=1.202+i0.562, γ=2.040, ϵ=0.391, χ^2=73.5)

K^- lab. momentum (Mev/c)	Cross sections (mb)							Production ratios			Phase
	σ_{el}	σ_{ce}	σ_0	σ_1	σ_{Σ^-}	σ_{Σ^+}	$\sigma_{\Sigma^0+\Lambda}$	$\Lambda/(\Sigma^0+\Lambda)$	Σ^-/Σ^+	$\frac{(\Sigma^-+\Sigma^+)}{(\Sigma^0+\Lambda)}$	$\phi_{\Sigma_0-\Sigma_1}$
at-rest	-	-	-	-	-	-	-	0.21	2.04	1.91	-63.2
37.5	1210.3	0.0	1451.9	371.0	409.2	187.7	314.6	0.23	2.18	1.90	-61.7
62.5	239.7	0.0	653.3	194.4	197.0	79.9	146.9	0.26	2.46	1.89	-59.0
87.5	115.8	0.0	331.8	157.6	122.4	36.2	86.1	0.36	3.38	1.84	-53.7
112.5	97.5	27.0	184.3	119.9	66.4	31.5	54.2	0.43	2.11	1.81	-68.4
137.5	82.9	24.5	130.0	86.2	42.3	27.3	38.5	0.44	1.55	1.81	-77.1
162.5	73.1	20.4	96.9	64.5	29.0	23.0	28.8	0.44	1.26	1.81	-83.2
187.5	65.6	16.7	75.0	49.8	20.8	19.4	22.3	0.44	1.07	1.81	-88.0
212.5	59.4	13.7	59.7	39.4	15.4	16.5	17.7	0.44	0.93	1.81	-92.0
237.5	54.2	11.3	48.6	31.8	11.8	14.1	14.3	0.43	0.83	1.81	-95.4
262.5	49.7	9.3	40.3	26.1	9.2	12.2	11.8	0.43	0.75	1.81	-98.4
287.5	45.8	7.8	33.9	21.7	7.3	10.6	9.9	0.43	0.69	1.81	-100.9

REFERENCES

1. Ronald R. Ross, Elastic-and Charge-Exchange Scattering of K^- Mesons in Hydrogen (thesis), Lawrence Radiation Laboratory Report UCRL-9749, August 1960 (unpublished).
2. R.H. Dalitz and S.F. Tuan, Ann. Phys. 10, 307 (1960).
3. T.B. Day, G.A. Snow, and J. Sucher, Phys. Rev. Letters 3, 61 (1959).
4. Luis W. Alvarez, The Interactions of Strange Particles, Lawrence Radiation Laboratory Report UCRL-9354, August 1960 (unpublished).
5. N. Horwitz, J.J. Murray, R.R. Ross, and R.D. Tripp, 450-Mev/c K^- and $\bar{p}$ Beams at the Northwest Target Area of the Bevatron Separated by the Coaxial Velocity Spectrometer, University of California Radiation Laboratory Report UCRL-8269, June 1958 (unpublished).
6. Joseph J. Murray, A Coaxial Static-Electromagnetic Velocity Spectrometer for High-Energy Particles, University of California Radiation Laboratory Report UCRL-3492, May 1957 (unpublished).
7. John N. Dyer, Analysis of the Bevatron K^- Beam by Means of an Emulsion Stack, University of California Radiation Laboratory Report UCRL-8364, July 1958 (unpublished).
8. M. Gell-Mann and A.H. Rosenfeld, Ann. Rev. Nuclear Sci. 7, 407 (1957).
9. Glenwood Clark, Jr. and William F. Diehl, Range-Energy Relation for Liquid-Hydrogen Bubble Chambers (M.S. Thesis), University of California Radiation Laboratory Report UCRL-3789, May 1957 (unpublished).
10. B. Cork, L. Kerth, W.A. Wenzel, J.W. Cronin, and R.W. Cool, Phys. Rev. 120, 1000 (1960).
11. P. Franzini, A. Garfinkel, J. Keren, A. Michelini, R. Plano, A. Prodell, M. Schwartz, J. Steinberger, and S.E. Wolf, Bull. Am. Phys. Soc. 5, 224 (1960).
12. A. Pais, On the Theory of Non-Leptonic Hyperon Decays, Lawrence Radiation Laboratory Report UCRL-9460, October 1960 (unpublished).

13. S.P. Rosen, Phys. Rev. Letters 6, 504 (1961).
14. Frank S. Crawford, Jr., Marcello Cresti, Myron L. Good, M. Lynn Stevenson, and Harold K. Ticho, Phys. Rev. Letters 2, 114 (1959).
15. F. Eisler, R. Plano, A. Prodell, N. Samios, M. Schwartz, J. Steinberger, P. Bassi, V. Borrelli, G. Puppi, H. Tanaka, P. Waloschek, V. Zoboli, M. Conversi, P. Franzini, I. Manelli, R. Santangelo, V. Silvestrini, G.L. Brown, D.A. Glaser, and C. Graves, Nuovo cimento 7, 222 (1958).
16. Jack Leitner, Paul Nordin, Jr., Arthur H. Rosenfeld, Frank T. Solmitz, and Robert D. Tripp, Phys. Rev. Letters 3, 238 (1959).
17. R. Gatto (Istituto di Fisica e Scuola di Perfezionamento in Fisica Nucleare, Istituto), private communication.
18. A.H. Rosenfeld, Proceedings of the International Conference on High Energy Accelerators and Instrumentation, (CERN Scientific Information Service, Geneva, 1959), pp. 533-541. Also, W.E. Humphrey, "A Description of the PANG Program", Alvarez Group Memos No. 111 and 115, Lawrence Radiation Laboratory (unpublished)
19. J. Peter Berge, Frank T. Solmitz, and Horace Taft, Rev. Sci. Instr. 32, 538 (1961).
20. Harold Cramér, The Mathematical Methods of Statistics (Princeton University Press, Princeton, 1946), pp. 498, 480.
21. Ulrich Kruse and Michael Nauenberg, S-Wave $\bar{K}$-N Scattering Amplitudes, Lawrence Radiation Laboratory Report, UCRL-8888 September 1959 (unpublished).
22. J.C. Jackson and H.W. Wyld, Phys. Rev. Letters 2, 355 (1959).
23. R.H. Dalitz, On the Strong Interactions of the Strange Particles, Lawrence Radiation Laboratory Report UCRL-9580, January 1961 (unpublished).

LEGAL NOTICE

This report was prepared as an account of Government sponsored work. Neither the United States, nor the Commission, nor any person acting on behalf of the Commission:

A. Makes any warranty or representation, expressed or implied, with respect to the accuracy, completeness, or usefulness of the information contained in this report, or that the use of any information, apparatus, method, or process disclosed in this report may not infringe privately owned rights; or

B. Assumes any liabilities with respect to the use of, or for damages resulting from the use of any information, apparatus, method or process disclosed in this report.

As used in the above, "person acting on behalf of the Commission" includes any employee or contractor of the commission, or employee of such contractor, to the extent that such employee or contractor of the Commission, or employee of such contractor prepares, disseminates, or provides access to, any information pursuant to his employment or contract with the Commission, or his employment with such contractor.